Symmetrical Diacetylenes Outfitted with Ionic Liquid-like Groups: Structural, Polymerization, and Carbonization Studies

Karim Fahsi, Xavier Dumail, Lydie Viau, Arie van der Lee, Nathalie Masquelez, Dominique Granier, Cyril Vaulot, Sylvain Georges Dutremez

Symmetrical diacetylenes outfitted with ionic liquid-like groups: structural, polymerization, and carbonization studies

Karim Fahsi,[†,‡] Xavier Dumail,[†] Lydie Viau,[§] Arie van der Lee,[‖] Nathalie Masquelez,[‖] Dominique Granier,[†] Cyril Vaulot,[⊥] and Sylvain Georges Dutremez*[,†]

* Corresponding author. E-mail: sylvain.dutremez@umontpellier.fr.

[†] ICGM, Université de Montpellier, CNRS, ENSCM, 34095 Montpellier Cedex 5, France.

[‡] Present address: Laboratoire de Chimie Organique Hétérocyclique, Faculté des Sciences, Université Mohammed V, Filière Technique de Santé à l'Institut Supérieur des Professions Infirmières et Techniques de Santé, 4 avenue Ibn Battouta BP 1014 RP, Rabat, Maroc.

[§] Institut UTINAM, UMR CNRS 6213, Equipe MSF, Université de Franche-Comté, 16 Route de Gray, 25030 Besançon, France.

[‖] IEM, Université de Montpellier, CNRS, ENSCM, 34095 Montpellier Cedex 5, France.

[⊥] Institut de Science des Matériaux de Mulhouse (IS2M), UMR 7361, 15 Rue Jean STARCKY, BP 2488, 68057 MULHOUSE Cedex, France.

ABSTRACT: Three symmetrical diacetylenes (DAs) bearing tetraalkylammonium substituents have been prepared, namely 1,6-bis(triethylammonium)hexa-2,4-diyne diiodide (**2**), dinitrate (**3**), and bis[bis(trifluoromethylsulfonyl)imide] (**4**). For these three salts, the duality between polymerization and carbonization has been investigated, and the results have been rationalized in terms of solid-state organization and molecular structure. These DAs have been irradiated at 254 nm with concomitant annealing at 80 °C (**4**) or 110 °C (**2** and **3**), and the lack of polydiacetylene (PDA) formation agrees with the fact that the C≡C-C≡C rods do not have a suitable orientation for 1,4-addition. Compound **4** is an ionic liquid. This DA starts melting at 88 °C with a maximum peak value of 104 °C, as ascertained by differential scanning calorimetry (DSC) and thermogravimetric (TG) analyses. It is stable in the liquid state at 120 °C for several hours and remains unchanged at 170 °C for a few minutes without any sign of PDA formation, which means that if some kind of organization exists in the liquid phase, it is not helpful for 1,4-polymerization. Thermolyses of **2**-**4** have been conducted under a nitrogen flow up to 220 °C (**3**) and 1200 °C (**2** and **4**). In all three cases, graphite-like carbon materials were obtained. The graphite-like structures start to form around 200 °C, that is the temperature where cycloaromatization of the triple bonds takes place. The residues from the pyrolyses of **2** and **4** exhibit nitrogen contents of 1.75 and 1.40 wt%, respectively, and powder X-ray diffraction and Raman analyses indicate that these materials have coherently scattering domain sizes in the range 1-3 nm depending on the crystallographic direction. The BET specific surface area of **2@1200** derived from dinitrogen sorption experiments is 88 m^2 g^{-1} and that of **4@1200** 33 m^2 g^{-1}. These values are much higher than those measured in previous work for carbon residues prepared at 1100 °C from imidazolium- and benzimidazolium-appended diacetylenes, thereby highlighting the pivotal influence of the size of the cation on the microstructure of the resulting carbon material. In addition, **2@1200** appears to be mostly microporous and **4@1200** mesoporous, which suggests that the anion also plays a central part in the structuring of the final solid. Last, X-ray Photoelectron Spectroscopy (XPS) analysis of **4@1200** indicates that, besides nitrogen, this residue also contains small amounts of fluorine and sulfur, thus making carbonization of ionic diacetylenes an alternative method to introduce doping elements in a graphite structure.

INTRODUCTION

Diacetylenes (DAs) are a unique class of molecules that have the ability to polymerize in the solid state, yielding π-conjugated 1D systems, the polydiacetylenes (PDAs).[1-6] For such a reaction to occur, a set of crystal packing requirements, compiled under the name ‘‘Topochemical Principle’’,[7] must be fulfilled (Scheme 1): (i) the translational period d of the monomer is in the range of 4.7 to 5.2 Å; (ii) R_v is smaller than 4 Å, with a lower limit of 3.4 Å; (iii) the angle γ between the diacetylene rod and the translational vector is close to 45°.[4,7-10] The upper limit for $R_{1,4}$ as quoted by Baughman is 5 Å,[2] but according to Huntsman, this limit should not be much greater than 4.3 Å.[10]

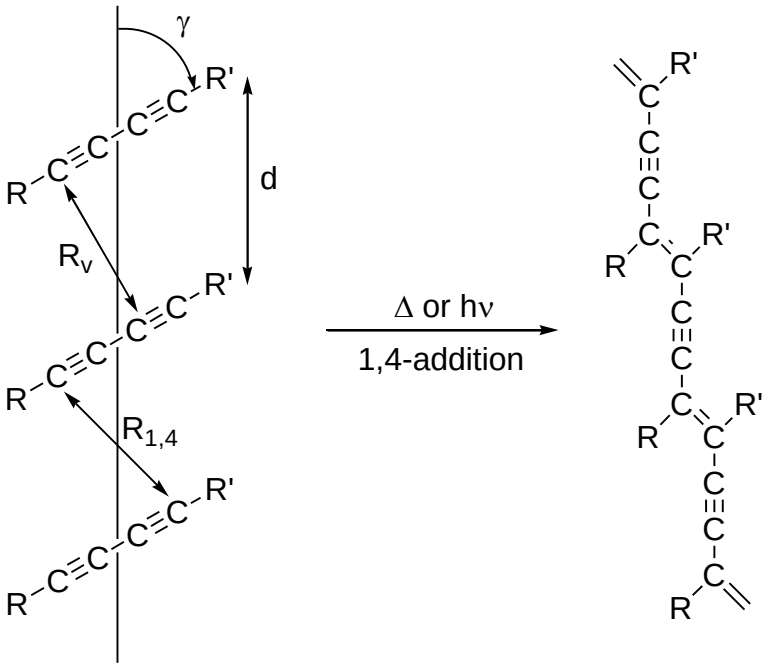

Scheme 1. Schematic representation of the topochemical principle for diacetylene polymerization

Technically, it is possible to bypass the hurdle stemming from the necessity of having the DA molecules suitably oriented in the solid state by carrying out diacetylene polymerization in the molten state. In 2003, we reported the results of a study concerning the thermolysis of $Me_3SiC{\equiv}CC{\equiv}CSiMe_3$ (Me = methyl) in the molten state in which we showed that short PDA chains with enyne and butatriene backbones were generated, despite the fact that the molecules did not have the correct orientation for diacetylene polymerization in the

solid state.[11] In parallel, it was found that thermolysis of $Me_3SiCH_2C{\equiv}CC{\equiv}CCH_2SiMe_3$ in the molten state gave polyaromatic structures. The dichotomy between these two diynes was ascribed to their unlike molecular structures, not to the existence of substantially different intermolecular interactions in the liquid.

A subtle way of setting the scene for diacetylene polymerization in the molten state is to introduce intermolecular interactions that create organized phases. Thus, in the past, several groups have described DA polymerization in liquid crystal phases.[12-16] The question then arises as to whether it would be possible to control the polymerization reactivity of ionic DAs by using molecules equipped with ionic liquid-like substituents. Indeed, ionic liquids (ILs) are considered to be organized media owing to the fact that they contain regions where aggregation is present.[17-23] Curiously, no literature is available on 1,4-polymerization of diacetylenic ionic liquids in the molten state, the closest reported study concerning the polymerization of 1,4-bis(4-benzylpyridinium)butadiyne triflate at 215 °C just after melting.[24,25] This temperature is way above the 100 °C threshold accepted for ionic liquids.

In years past, our group has also been involved in studying the polymerization of ionic DAs equipped with ionic liquid-like groups. In particular, we reported recently the syntheses of imidazolium- and benzimidazolium-appended diacetylenes with dicyanamide and tricyanomethanide counterions and showed that these compounds did not polymerize in the solid state.[26] Unfortunately, these salts were not meltable, so their polymerization could not be studied in the molten state. However, by replacement of the dicyanamide and tricyanomethanide anions with bromide, it is possible to turn the imidazolium-containing precursor into a photochemically reactive species and prepare an ionic PDA from it.[27] But, like its dicyanamide and tricyanomethanide counterparts, this diacetylene is unreactive thermally and has no melting point.

The first aspect of this paper deals with the study of the polymerization reactivity of ionic DAs outfitted with tetraalkylammonium substituents. Numerous examples exist in the literature of tetraalkylammonium salts that are ionic liquids,[22] and furthermore, ethyl- and diethylammonium nitrate are among the first ionic liquids ever reported.[28] Specifically, 1,6-bis(triethylammonium)hexa-2,4-diyne diiodide (**2**), dinitrate (**3**), and bis[bis(trifluoromethylsulfonyl)imide] (**4**) have been prepared by derivatization of 1,6-bis(diethylamino)hexa-2,4-diyne (**1**) as shown in Scheme 2. The solid-state polymerization reactivities of diynes **2**-**4** have been assessed by irradiation at 254 nm with concomitant annealing at 80 °C (**4**) or 110 °C (**2** and **3**), and the results have been correlated with the X-ray crystal structures of these salts. Furthermore, DSC and TG analyses show that **2** and **3** are not

meltable and that **4** is an ionic liquid. So, the molten-state polymerization of this latter diacetylene has been studied at 120 and 170 °C, and the outcome of this investigation is reported here.

The second part of this work deals with carbon materials. In the last fifteen years, several groups have focused their attention towards the synthesis of carbonaceous materials from ionic precursors, especially ionic liquids. The goal of these investigations was to prepare chars showing high specific surface areas, high nitrogen contents, high electrical conductivities, and possessing excellent electrocatalytic activities. These kinds of materials are important in domains such as energy storage, electrochemistry, gas sequestration, and catalysis.[29] To this end, three main strategies have been developed: in a first approach, imidazolium cations equipped with nitrile groups were employed, as nitrile groups polymerize upon heating and then transform into N-containing graphitic carbon.[30-34] In a second approach, anions possessing C≡N groups such as dicyanamide, tricyanomethanide, and tetracyanoborate anions were used, because these anions polymerize in the same way as the preceding cations and are commercially available.[31-40] The third methodology consists in the utilization of protic ionic liquids (PILs) and protic salts (PSs) as precursors. These precursors were synthesized by protonation of aliphatic or aromatic amines with various organic and inorganic acids.[41,42]

Our group has also studied the preparation of carbon materials from ionic precursors. Besides the assessment of the solid-state polymerization reactivities of the aforementioned imidazolium- and benzimidazolium-appended DAs equipped with dicyanamide and tricyanomethanide anions, these salts were thermolyzed at 1100 °C in an argon flow.[26] It was found that graphite-like carbon materials resulted from these thermolyses with yields up to 50% and nitrogen contents as high as 6.6%. These results were ascribed to the joint effects of polymerization of the C≡N groups of the anions and cycloaromatization of the triple bonds of the cations. Unfortunately, the solids showed very low BET specific surface areas, in the range of 0.36 to 3.43 $m^2\ g^{-1}$, which precluded their use as catalysts in electrocatalytic reactions such as ORR (oxygen reduction reaction) and OER (oxygen evolution reaction).[34]

Herein we show that ionic DAs **2-4** can be used as precursors for the preparation of graphitic carbon. The pyrolytic materials resulting from thermolysis of **2** and **4** at 1200 °C, hereafter denoted as **2@1200** and **4@1200**, exhibit BET specific surface areas that are much higher than those of the carbon residues prepared from the aforesaid imidazolium- and benzimidazolium-containing salts,[26] thereby underscoring the vital influence of the size of the

cation on the microstructure of the resulting carbon material.[36] Furthermore, the microstructures of **2@1200** and **4@1200** are different, which suggests that the anion also participates in the structuring of the final solid. Last, X-ray Photoelectron Spectroscopy (XPS) analysis of **4@1200** indicates that not only nitrogen but also fluorine and sulfur are present in the resulting carbonaceous material, which makes carbonization of ionic diacetylenes an alternative method to incorporate doping elements in a graphite structure.

EXPERIMENTAL SECTION

C**haracterization Methods.** Solution ^{1}H, ^{13}C, and ^{19}F NMR spectra were obtained on a Bruker Avance 400 MHz instrument equipped with a BBFO probehead or a Bruker Avance III 500 MHz instrument equipped with a helium-cooled BBFO cryoprobe. Chemical shifts were referenced as follows: ^{1}H nucleus (protio impurities of the NMR solvents), ^{13}C nucleus (NMR solvents), ^{19}F nucleus ($CFCl_3$). Solid-state ^{1}H and ^{13}C magic-angle spinning (MAS) NMR spectra were recorded on a Varian VNMRS 600 spectrometer operating at 14.1 T (^{1}H frequency = 600 MHz and ^{13}C frequency = 151 MHz). A 3.2 mm Varian T3 HXY MAS probe equipped with a KelF module was used. The samples were spun in zirconia rotors fitted with Vespel® caps. The spinning frequencies were 20 or 24 kHz for ^{1}H NMR analyses and 12 kHz for ^{13}C NMR analyses. Chemical shifts were referenced to an external sample of adamantane (low frequency peak (CH_2) at δ = 1.8 ppm for ^{1}H NMR analysis; high frequency peak (CH_2) at δ = 38.5 ppm for ^{13}C NMR analysis). Raman spectra with λ_{ex} = 1064 nm were measured at room temperature on a Bruker RFS100 FT spectrometer, and Raman data with λ_{ex} = 785 nm were obtained on a Renishaw inVia instrument. ESI mass spectra were recorded on a Bruker micrOTOF-Q II spectrometer or a Waters Synapt G2-S instrument. High-temperature (up to 1200 °C) coupled TG-DSC experiments were carried out under a nitrogen flow (100 mL min^{-1}) on a TA Instruments SDT-Q600 Simultaneous TGA / DSC apparatus, with a heating rate of 10 °C min^{-1}. X-ray powder patterns were recorded on a PANalytical X'pert MPD-Pro diffractometer in the Bragg-Brentano θ-θ reflection geometry with Ni-filtered Cu Kα radiation (λ = 1.5418 Å). To avoid any interference line from the sample holder, the well ground calcined powders were placed on a zero background silicon plate. Measurements were performed at room temperature in the 3-60° 2θ range, using a step size of 0.033° and a counting time per step of 240 s. C, H, N elemental analyses were performed in-house using a Thermo Finnigan FLASH EA 1112 Series analyser or an Elementar Vario Micro Cube apparatus. XPS analyses were carried out using a Thermo Electron ESCALAB 250 apparatus equipped with a monochromatic Al Kα source (hν = 1486.6 eV). Surface areas of about 0.15 mm^2 were scanned. The background signal was removed using the Shirley method.[43] Surface atomic concentrations were determined from peak areas using the atomic sensitivity factors reported by Scofield.[44] Binding energies (BE) of all core levels are calibrated with respect to the C=C C1s peak at 284.4 eV. Surface charging effects were compensated by use of a low-energy electron beam (–2 eV).

Materials. The chemicals used in this study were obtained from the following commercial sources: diethylamine (Sigma-Aldrich), iodoethane (Alfa Aesar), silver nitrate (Alfa Aesar), lithium bis(trifluoromethylsulfonyl)imide (IoLiTec). Solvents were purchased from the following suppliers: dichloromethane (Carlo Erba), diethyl ether (Fisher), methanol (VWR), acetonitrile (Sigma-Aldrich), HPLC water (Merck). Prior to use, dichloromethane and acetonitrile were refluxed over and distilled from calcium hydride. 2,4-Hexadiyne-1,6-diol bis(*p*-toluenesulfonate) was made from 2,4-hexadiyne-1,6-diol according to a known procedure.[45] 2,4-Hexadiyne-1,6-diol was prepared by oxidative dimerization of propargyl alcohol according to reported protocols.[46,47]

Synthesis. *1,6-Bis(diethylamino)hexa-2,4-diyne (**1**).* A homogeneous solution made of 2,4-hexadiyne-1,6-diol bis(*p*-toluenesulfonate) (5.3 g, 12.6 mmol), diethylamine (3.88 g, 53.2 mmol, 4.2 equiv), and 150 mL of dry CH_2Cl_2 was prepared. The mixture was stirred overnight under reflux. After cooling to room temperature, the solution was concentrated to a small volume (20 mL). The organic phase was washed with a 500 mL aliquot of a 1 M aqueous NaOH solution, and the two layers were separated. The aqueous phase was extracted with diethyl ether (3 × 300 mL). The organic layer was dried over magnesium sulfate, and the solvent was removed on a rotary evaporator. The resulting brown oil was purified by flash chromatography using a Biotage® Isolera™ One Flash Purification System. 50g Biotage® SNAP Ultra cartridges packed with Biotage® HP-Sphere™ 25μm silica gel beads were used, along with a CH_2Cl_2-CH_3OH solvent mixture. The following elution scheme was employed during purification: 100:0 v/v, then 90:10 v/v, and finally 80:20 v/v. Diacetylene **1** was obtained as a brown oil (1.8 g, 65%). ^{1}H NMR (400 MHz, $CDCl_3$): δ 1.05 (t, J = 7.2 Hz, 12H, H_5), 2.55 (q, J = 7.2 Hz, 8H, H_4), 3.49 (s, 4H, H_3). ^{13}C NMR (101 MHz, $CDCl_3$): δ 12.8 (C_5), 41.4 (C_3), 47.6 (C_4), 69.6 (C_1), 73.2 (C_2). Raman (neat liquid): $\tilde{\nu}$ 2243 cm^{-1}. HRMS (ESI+): m/z calculated for $C_{14}H_{25}N_2$ $[M+H]^+$: 221.2018. Found: 221.2017.

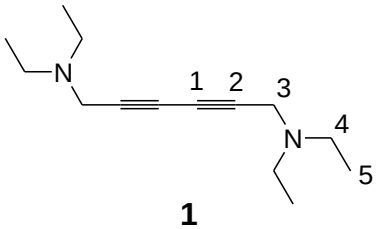

1

*1,6-Bis(triethylammonium)hexa-2,4-diyne diiodide (**2**).* A large excess of iodoethane (1.5 g, 9.62 mmol) was mixed with **1** (0.508 g, 2.31 mmol) in distilled acetonitrile (60 mL). The homogeneous solution was stirred for 48 h at room temperature under an inert atmosphere. The beige solid that precipitated out was filtered off, and the filtrate was stirred for another 48 h at room temperature with a second portion of iodoethane (1.5 g, 9.62 mmol). The newly formed solid was collected and combined with the first fraction. The entire solid was washed with cold acetonitrile and dried *in vacuo* (0.860 g, 69%). ^{1}H NMR (400 MHz, D_2O): δ 1.37 (t, J = 7.2 Hz, 18H, H_5), 3.49 (q, J = 7.2 Hz, 12H, H_4), 4.40 (s, 4H, H_3). ^{13}C NMR (101 MHz, D_2O): δ 7.0 (C_5), 48.1 (C_3), 53.9 (C_4), 68.2 (C_1), 73.2 (C_2). Raman (neat powder): $\tilde{\nu}$ 2263 cm^{-1}. HRMS (ESI+): *m*/*z* calculated for $C_9H_{17}N$ [1/2(*M*–2I)]$^+$, $C_{18}H_{34}IN_2$ [*M*–I]$^+$: 139.1356, 405.1761. Found: 139.1370, 405.1765. HRMS (ESI–): *m*/*z* calculated for I$^-$, $C_{18}H_{34}I_3N_2$ [*M*+I]$^-$, $C_{36}H_{68}I_5N_4$ [2*M*+I]$^-$: 126.9050, 658.9862, 1191.0673. Found: 126.9057, 658.9859, 1191.0645. Anal. Calcd for $C_{18}H_{34}I_2N_2$: C, 40.62; H, 6.44; N, 5.26%. Found: C, 40.73; H, 6.53; N, 5.63%.

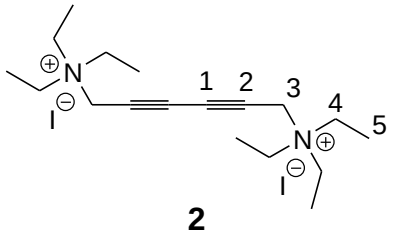

2

*1,6-Bis(triethylammonium)hexa-2,4-diyne dinitrate (**3**).* Compound **2** (0.404 g, 0.76 mmol) was dissolved in HPLC water (14 mL), and solid silver nitrate (0.25 g, 1.47 mmol, 1.94 equiv) was added to this solution. A suspension quickly formed that was stirred overnight at room temperature. The major part of the precipitate was removed by suction filtration. Remaining traces of silver iodide were eliminated by filtration of the filtrate through a syringe filter. The filtrate was concentrated to dryness by lyophilization. A beige solid was obtained (0.265 g, 87%). ^{1}H NMR (400 MHz, D_2O): δ 1.35 (t, J = 7.2 Hz, 18H, H_5), 3.46 (q, J = 7.2 Hz, 12H, H_4), 4.37 (s, 4H, H_3). ^{13}C NMR (101 MHz, D_2O): δ 6.9 (C_5), 47.9 (C_3), 53.8 (C_4), 68.1 (C_1), 73.0 (C_2). Raman (neat powder): $\tilde{\nu}$ 2263 cm^{-1}. HRMS (ESI+): *m*/*z* calculated for $C_{16}H_{29}N_2$ [*M*–2NO_3–C_2H_5]$^+$, $C_{18}H_{34}N_3O_3$ [*M*–NO_3]$^+$, $C_{36}H_{68}N_7O_9$ [2*M*–NO_3]$^+$: 249.2331, 340.2600, 742.5079. Found: 249.2330, 340.2595, 742.5083. HRMS (ESI–): *m*/*z* calculated for NO_3^-, $C_{18}H_{34}N_5O_9$ [*M*+NO_3]$^-$: 61.9878, 464.2357. Found: 61.9877, 464.2353. Anal. Calcd for $C_{18}H_{34}N_4O_6$: C, 53.71; H, 8.51; N, 13.92%. Found: C, 53.50; H, 8.40; N, 13.79%.

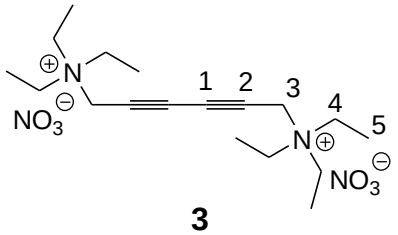

3

*1,6-Bis(triethylammonium)hexa-2,4-diyne bis[bis(trifluoromethylsulfonyl)imide] (**4**).* Compound **2** (0.25 g, 0.47 mmol) was dissolved in a 7 mL portion of HPLC water. Separately, a solution of lithium bis(trifluoromethylsulfonyl)imide (0.27 g, 0.94 mmol, 2.0 equiv) in HPLC water (8 mL) was prepared. The lithium bis(trifluoromethylsulfonyl)imide solution was added dropwise to the solution containing **2**. Quickly, a suspension formed, which became thicker with time. Stirring was continued for 24 h at room temperature. The beige precipitate was collected by suction filtration and washed with three aliquots of HPLC water (5-6 mL each time). The solid was dried *in vacuo* (0.35 g, 89%). ^{1}H NMR (400 MHz, CD_3CN): δ 1.27 (t, J = 7.2 Hz, 18H, H_5), 3.33 (q, J = 7.2 Hz, 12H, H_4), 4.17 (s, 4H, H_3). ^{19}F NMR (377 MHz, CD_3CN): δ –80.1 (s, 12F, CF_3). ^{13}C NMR (101 MHz, CD_3CN): δ 6.7 (C_5), 48.0 (C_3), 53.8 (C_4), 67.9 (C_1), 72.9 (C_2), 121.7 (q, J = 320 Hz, CF_3). Raman (neat powder): $\tilde{\nu}$ 2274 cm^{-1}. HRMS (ESI+): *m*/*z* calculated for $C_{20}H_{34}N_3O_4F_6S_2$ [M–N$(SO_2CF_3)_2$]$^+$: 558.1895. Found: 558.1899. HRMS (ESI–): *m*/*z* calculated for $C_2NO_4F_6S_2$ [N$(SO_2CF_3)_2$]$^-$: 279.9173. Found: 279.9178. Anal. Calcd for $C_{22}H_{34}N_4O_8F_{12}S_4$: C, 31.50; H, 4.09; N, 6.68%. Found: C, 31.52; H, 4.13; N, 6.39%.

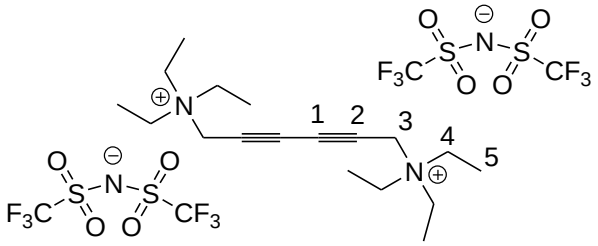

4

Single-Crystal X-ray Diffraction. Single crystals of **2** and **3** were obtained by allowing methanol solutions to evaporate slowly to dryness. Single crystals of **4** were grown from ethyl acetate. Crystal evaluation and intensity measurements for **4** were performed at –100 °C on a Bruker Venture diffractometer equipped with a Cu-*K*α microsource and a Photon-II detector. The APEX3 program was used for data collection, and the SAINT,

XPREP, and SADABS routines were respectively utilized for integration of the data using default parameters, empirical absorption correction using spherical harmonics employing symmetry-equivalent and redundant data, and correction for Lorentz and polarization effects.[48] Crystal evaluation and data collection for **2** and **3** were conducted at −100 °C with the CrysAlis PRO software package[49] on a Rigaku Oxford Diffraction Xcalibur-1 diffractometer equipped with a graphite-monochromated sealed-tube Mo-*K*α X-ray source. This same package was used for integration of the data frames using default parameters, correction for Lorentz and polarization effects, and for empirical absorption correction using spherical harmonics employing symmetry-equivalent and redundant data.

All three crystal structures were solved with the *ab initio* iterative charge-flipping method with parameters described elsewhere,[50] by using the SUPERFLIP program.[51] The structural models of **2** and **4** were refined against $|F|$ using full-matrix non-linear least-squares procedures as implemented in CRYSTALS[52] on all independent reflections with $I > 2\sigma(I)$. The structural model of **3** was refined against F^2 on all independent reflections with $I > -3\sigma(I)$. Hydrogen atoms were refined with riding constraints in all three structures.[53]

Crystallographic parameters and basic information pertaining to data collection and structure refinement are summarized in Table 1. Structural drawings were prepared with the three-dimensional graphical visualization program OLEX2.[54]

Microscopy. The carbon samples were placed in a mortar and a few drops of ethanol were added. The slurry was ground gently with a pestle in order to homogenize coarsely the size of the particles. A small amount of the slurry was drawn with a micropipette, and one drop was placed on a lacey carbon coated 300 mesh copper grid (from Agar Scientific). The grid was left to dry in air.

High-resolution transmission electron microscopy (HRTEM) micrographs were recorded using a Jeol JEM-2200FS microscope equipped with a 200 kV field emission gun (FEG) and an in-column energy filter (Omega filter). This equipment is part of the Microscopie Électronique et Analytique (MEA) instrumentation platform, Université de Montpellier, Montpellier, France.

Gas Sorption Studies. The gas-sorption properties of **2@1200** and **4@1200** were evaluated on a Micromeritics ASAP 2420 volumetric gas sorption analyzer. The adsorption/desorption experiments were carried out at −196 °C (liquid nitrogen temperature)

for N_2 and 0 °C (ice bath) for CO_2. The isotherms were measured in the relative pressure range p/p° of 0-1 for N_2 ($p°_{N2}$ = 760 mmHg at –196 °C) and 0-0.03 for CO_2 ($p°_{CO2}$ = 26141.72 mmHg at 0 °C). The samples were first outgassed under a vacuum of 1 μmHg at 300 °C for 12 h, then outgassed a second time at 300 °C for 2 h directly on the analysis port, just before testing. The free volumes were determined after each analysis to avoid adventitious contamination of the carbon materials. Due to the microporous and ultra-microporous natures of the samples, low pressure doses, 2 cm^3 g^{-1} STP for N_2 and 0.1 cm^3 g^{-1} STP for CO_2, were used so as to monitor more closely the adsorption at very low pressure.

The specific surface area was calculated by using the Brunauer, Emmett and Teller (BET) equation (S_{BET} in Table 4). The range of application of this equation was determined as follows: the upper p/p° limit was set at a relative pressure corresponding to the maximum of the Rouquerol curve, with a maximum value of 0.3. The lower limit was set at the most extreme point of the linear region of the BET transform so as to obtain a correlation coefficient equal to or greater than 0.9999, with a minimum p/p° value of 0.01. Evaluation of the microporous part from N_2 sorption results was performed with the *t*-plot model using a thickness range from 0.354 nm (thickness of a N_2 layer) to the highest possible value so that an acceptable coefficient of determination was obtained for the regression line, at least R^2 = 0.95. Finally, the pore size distribution (PSD) was determined by applying Density Functional Theory (DFT) calculations to the N_2 and CO_2 isotherms. The geometry of the pores was established for each sample by comparing the experimental isotherm with the DFT calculated one. In each case, the best fit (at high and low pressures), the lowest error of fit, and the smoothest calculated curve were sought. Optimal smoothing of the distribution was performed based on the intersection of the Roughness distribution versus regularization coefficient curve with the Root Mean Square RMS error versus regularization coefficient curve.

RESULTS AND DISCUSSION

Synthesis. The synthesis route for compounds **1-4** is featured in Scheme 2. Previous work in our group has shown that the preparation of 1,6-bis(1-imidazolyl)-2,4-hexadiyne by oxidative dimerization of 1-propargylimidazole following the Hay coupling protocol was problematic, as deactivation of the catalyst occurred during the reaction due to complexation of the copper ions by the imidazolyl groups.[55] As a result, this diyne was made by the reaction between 2,4-hexadiyne-1,6-diol bis(*p*-toluenesulfonate) and excess imidazole.[55,56] Here, 1,6-bis(diethylamino)hexa-2,4-diyne (**1**) was prepared in a similar way by allowing 2,4-hexadiyne-1,6-diol bis(*p*-toluenesulfonate) to react with a slight excess of diethylamine. The second step consists in the quaternization of the amino groups of **1** with excess iodoethane, giving **2** in 69% isolated yield. Salts **3** and **4** were prepared in 87% and 89% yield respectively by anion metatheses of **2** with silver nitrate and lithium bis(trifluoromethylsulfonyl)imide.

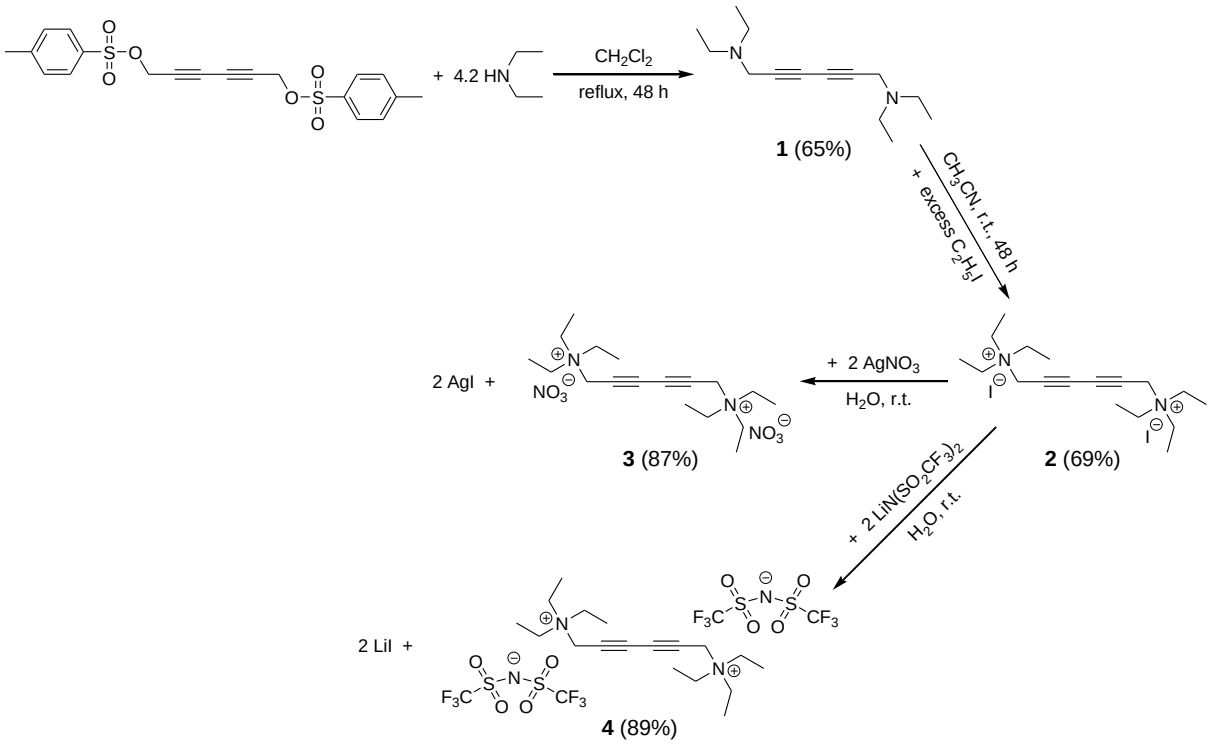

Scheme 2. Syntheses of compounds 1-4

Single-Crystal X-ray Diffraction Studies. *Structure of 2*. Compound **2** crystallizes in the monoclinic space group $P2_1/c$ with $Z = 2$ (Table 1). There is one half of a diacetylene

dication in the asymmetric unit and one iodide anion. When viewing the structure down the *b* axis (Figure 1), parallel stacks of DA rods are visible along with columns of iodide anions. This situation is similar to that previously observed for cationic DAs with imidazolium and benzimidazolium substituents.[26,27] Iodide anions are located in channels formed by three DA stacks. The distance between two successive DA cations in these stacks is 6.819 Å, and this distance is the same between iodide anions. Each I^- interacts with surrounding ammonium groups *via* C-H···I hydrogen bonds (Figure 2). There are three H···I contacts smaller than the sum of the van der Waals radii (3.18 Å): 3.066, 3.069, and 3.148 Å. These three interactions, which involve only methylene hydrogens, are a bit shorter than those detected in tetraethylammonium iodide, 3.182 and 3.243 Å.[57,58] In addition, intermolecular contacts are observed between ethyl protons and C_{sp} carbons, $d(CH_2\cdots C\equiv)$ = 2.900 Å and $d(CH_3\cdots C\equiv)$ = 2.807 Å, which suggests the presence of C-H···π interactions between neighboring DA cations in a given column. The $R_{1,4}$ distance between C_{sp} carbons susceptible of getting linked is 5.389 Å and the angle γ is 52.29° (Scheme 1). These values lie outside the accepted range,[4,7-10] meaning that this diacetylene should not polymerize in the solid state.

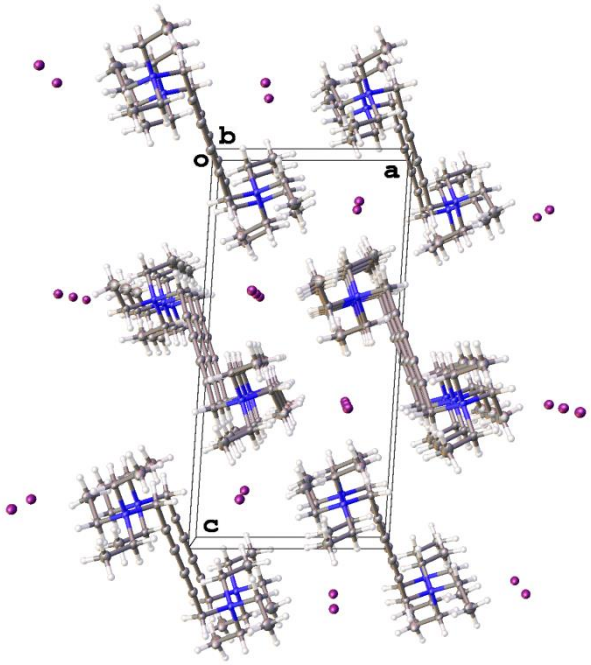

Figure 1. View along the *b* axis showing the organization of **2** in the solid state.

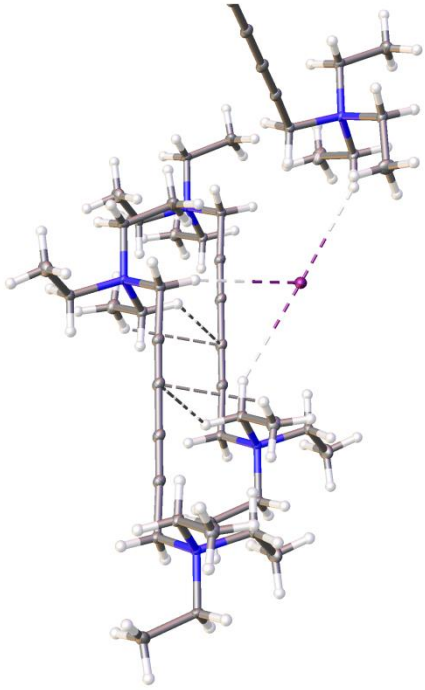

Figure 2. Charge-assisted hydrogen bonds and C-H···π interactions in crystalline **2**.

*Structure of **3***. Compound **3** crystallizes in the monoclinic space group $P2_1/n$ with Z = 4 (Table 1). There is one diacetylene dication in the asymmetric unit and two nitrate anions. The 3D organization of **3** is very much like that of **2**. When viewing the structure down the *b* axis (Figure 3), parallel stacks of DA rods are visible along with columns of nitrate anions. As in **2**, nitrate anions are located in channels formed by three DA stacks. The distance between two successive DA cations in these stacks is 6.854 Å, and this distance is the same between nitrate anions. The structure is sustained by numerous interactions between nitrate anions and alkyl groups. All types of alkyl groups are involved in these interactions, the two kinds of methylene groups and the methyl groups. In total, twenty NO_3^-···H-C charge-assisted hydrogen bonds are detected with distances spanning the range 2.254-2.711 Å (Figure 4). These distances are in line with those found in tetraethylammonium nitrate tris(thiourea), 2.400-2.511 Å.[59] Unlike **2**, no intermolecular contacts are detected between alkyl protons and C_{sp} carbons, consistent with the absence of C-H···π interactions between neighboring DA cations. The $R_{1,4}$ distance between C_{sp} carbons susceptible of getting linked is 5.921 Å and the angle γ is 59.89° (Scheme 1). These values differ significantly from the optimal ones,[4,7-10] meaning that this diacetylene should not polymerize in the solid state.

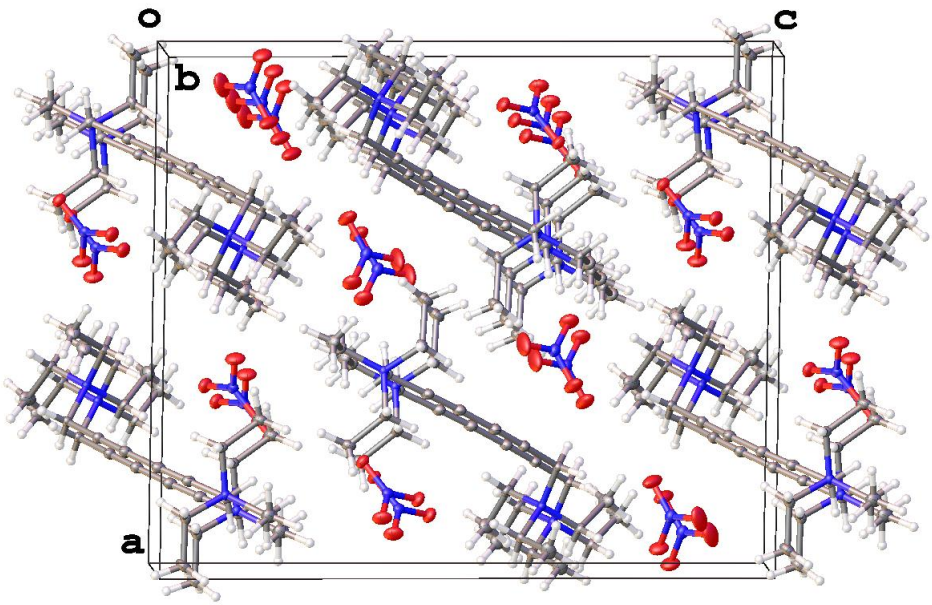

Figure 3. View along the *b* axis showing the organization of **3** in the solid state.

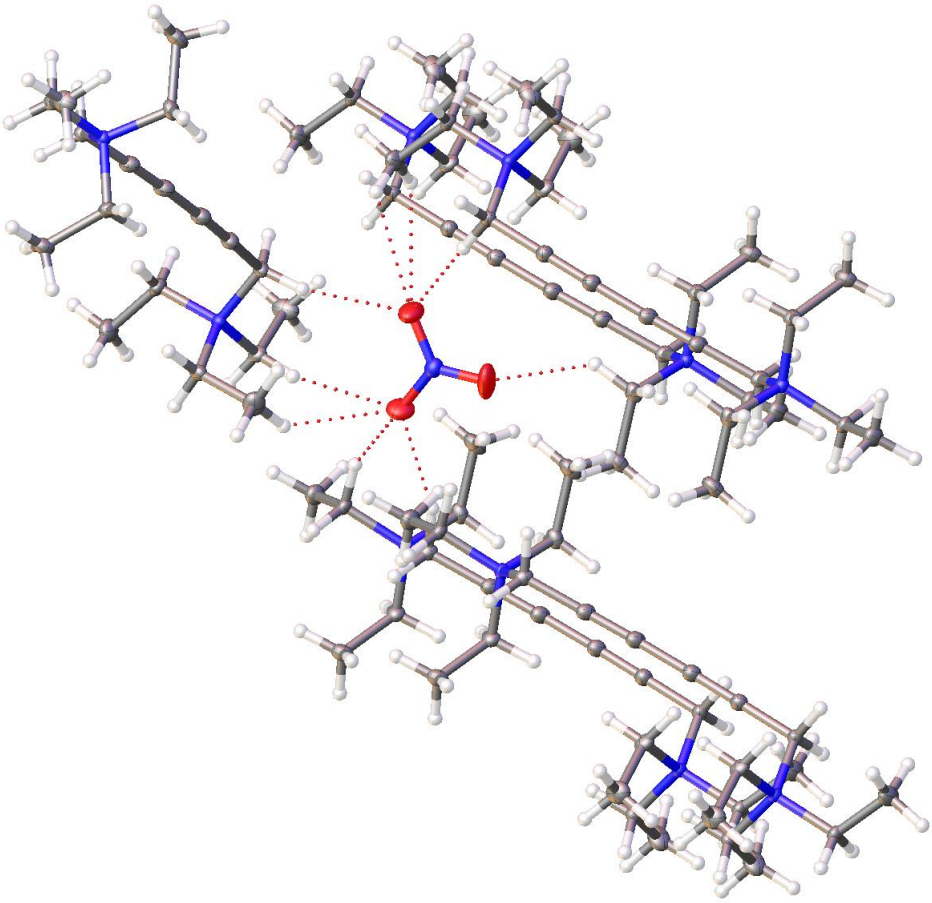

Figure 4. H-bond interactions between one nitrate anion and five DA molecules.

*Structure of **4***. Compound **4** crystallizes in the monoclinic space group $P2_1/n$ with Z = 2 (Table 1). There is one half of a diacetylene dication in the asymmetric unit and one bis(trifluoromethylsulfonyl)imide ($TFSI^-$) anion. The $TFSI^-$ anion has almost σ_v symmetry, contrasting with the low-energy conformations with C_2 and C_1 symmetries reported by Trulove.[60] In a similar way to **2** and **3**, the structure of **4** shows segregation between cations and anions. Upon looking at the unit cell down the *c* axis (Figure 5), stacks of DA rods are noticeable, which, this time, are not all parallel. The distance between two successive DA cations in these stacks is quite long, 11.426 Å, which excludes the possibility of having intrastack C-H$\cdots\pi$ interactions. $TFSI^-$ anions are located in channels formed by four DA stacks. Each channel contains two facing rows of anions, the distance between anions in each row being 11.426 Å. The structure is sustained by numerous hydrogen bonds between anions and cations; all types of alkyl groups participate in these interactions. There are five C-H$\cdots$O contacts in the range 2.384-2.720 Å, two of them belonging to C≡C$CH_2\cdots$O connections (d(H$\cdots$O) = 2.384 and 2.434 Å). There is one C-H$\cdots$N interaction with d(H$\cdots$N) = 2.618 Å and three C-H$\cdots$F contacts spanning the range 2.620-2.665 Å. Furthermore, there is one short F$\cdots$F contact between $TFSI^-$ anions with a distance of 2.716 Å. The crystal structure of tetraethylammonium bis(trifluoromethylsulfonyl)imide is known,[60] but since the $TFSI^-$ anions in this structure are heavily disordered, no meaningful comparison with the structure of **4** is possible. The $R_{1,4}$ distance between C_{sp} carbons susceptible of getting linked is 11.487 Å and the angle γ is 81.27° (Scheme 1). These values are way off the optimal criteria for solid-state polymerization of the diyne units.[4,7-10]

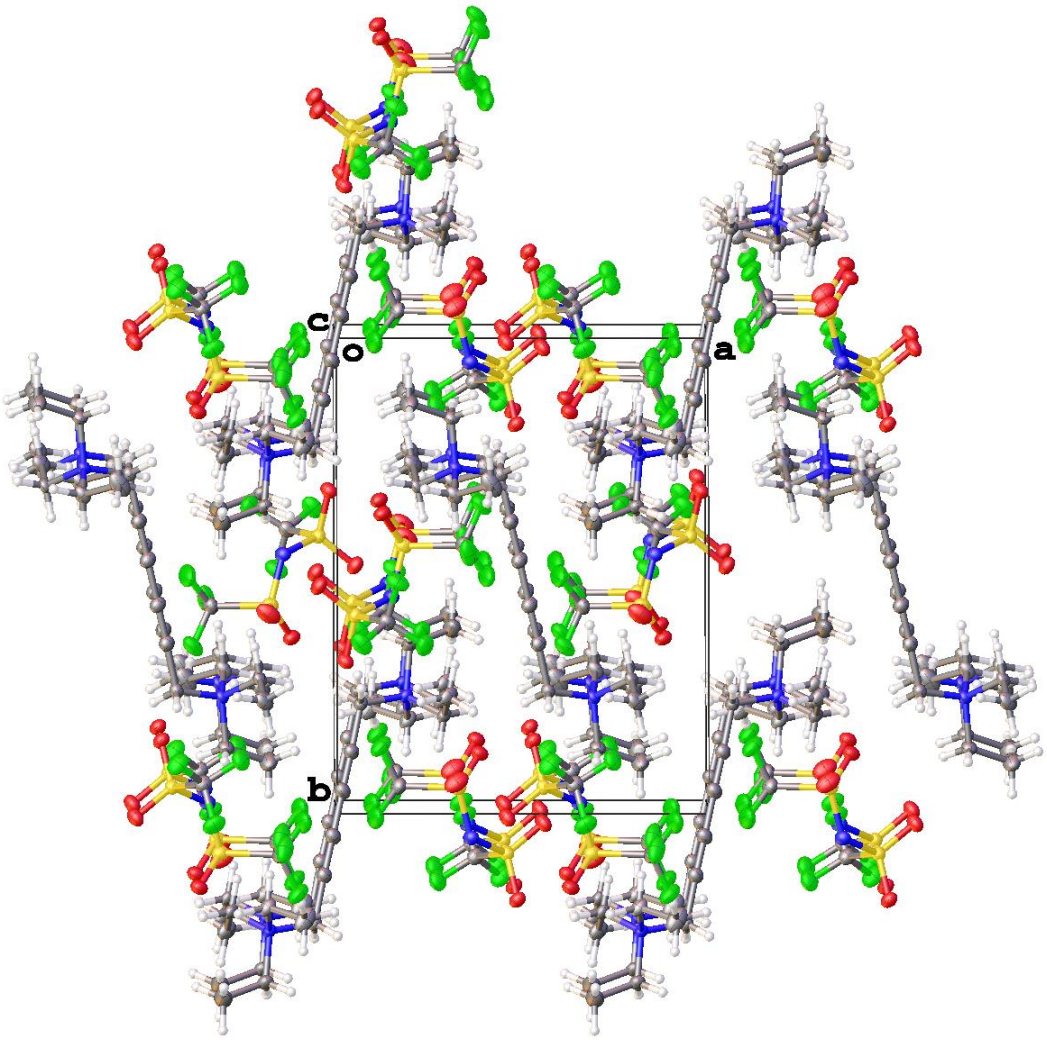

Figure 5. View along the *c* axis showing the organization of **4** in the solid state.

Hirshfeld surface analysis. A Hirshfeld surface analysis of compounds **2**-**4** was carried out using version 21.5 of the CrystalExplorer visualization tool.[61-63] The percentage contributions to the Hirshfeld surface area for various close intermolecular contacts involving the hydrogen atoms of the diacetylene fragments are shown in Figure 6. As can be seen, H···X (X = H, C, N, O, S, F, I) interactions are associated with about 90% of the overall Hirshfeld surface area of each cation. For compound **2**, C-H···I hydrogen bonds prevail and are associated with 13.6% of the interaction surface, whereas C-H···C contacts account for 6.8%. The remaining percentage, 70.1%, corresponds to H···H contacts. The fact that this salt has the highest percentage of C-H···C contacts among the three compounds being studied certainly has to do with the presence of C-H···π interactions (see above). Unsurprisingly, Hirshfeld surface analysis of salt **3** indicates that C-H···O interactions dominate and are

associated with a large part of the surface area, 29.3% (see Figure 6). Other interactions such as C-H···N and C-H···C contacts have much smaller contributions to the overall surface, 1.1 and 5.2%, respectively. With regard to non-bonding H···H interactions, these interactions account for 54.7% of the surface. The situation of diacetylene **4** is quite interesting. It was anticipated from the point-by-point structural description made previously that C-H···O interactions would represent a large fraction of the Hirshfeld surface area, and the calculated value of 31.1% confirms that this is indeed the case. However, what was less expected is the fact that C-H···F interactions would be associated with an even larger fraction of the Hirshfeld surface area, 33.6%. Close inspection of the structure had indeed shown that C-H···F hydrogen bonds were important, but their contribution to the cohesion of the crystal lattice could not be evaluated precisely. Such a major piece of information would have gone unnoticed without performing a Hirshfeld surface analysis. In parallel, other interactions such as C-H···C, C-H···N, and C-H···S interactions have marginal contributions (3.0, 3.5, and 0.1%, respectively), and H···H contacts account for 20.3% of the surface. So, altogether, C-H···O interactions and C-H···F contacts represent 64.7% of the Hirshfeld surface area of the ammonium cation of **4**, and we believe this situation reinforces the presumption that this diacetylene exists as an ion pair in the molten state (see below).

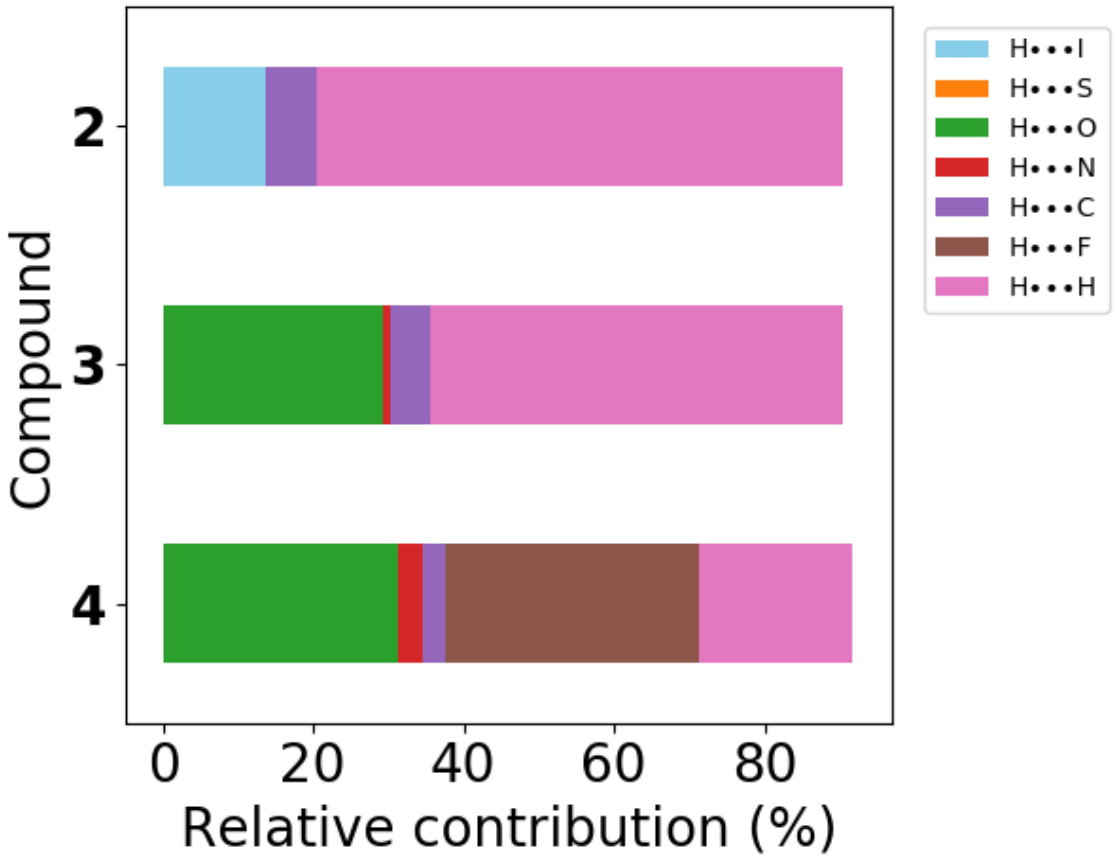

Figure 6. Relative contributions of various intermolecular interactions to the Hirshfeld surface areas of the diacetylenic cations in compounds **2-4**.

Thermal Behavior. The thermal behavior of compounds **2-4** was studied by coupled TG-DSC analysis under a nitrogen flow. Diacetylenes **2** and **4** were heated to 1200 °C, while **3** was thermolyzed to just 220 °C because of the presence of nitrate ions. The TG and DSC thermograms of **2** are shown in Figures 7(a) and 7(b). A first exothermic event is observed in the range 183-240 °C with a peak maximum at 213 °C. This sharp phenomenon is accompanied by a weight loss of 38.8%. No melting is observed prior to this event (no endotherm is detected by DSC). A second weight loss is detected just after the first one in the range 240-357 °C with a peak maximum of 313 °C. However, unlike the first event, this second phenomenon is endothermic. This endotherm is reminiscent of those observed in the DSC thermograms of liquid crystals and might correspond to some sort of phase transition in close conjunction with the decomposition of the compound. Subsequently, decomposition continues in a gradual manner with no distinct step in the TG curve; at 1200 °C, a carbonaceous material is obtained in 10.6% yield. When compared with the molecular weight

of the starting compound, the amount of residue corresponds to the recovery of 4.7 carbon atoms. Quite likely, most of these atoms originate from the C≡C-C≡C units due to cyclotrimerization of these units upon thermolysis.[11,26,64,65] This hypothesis is corroborated by the fact that simple alkylammonium iodides undergo complete volatilization upon heating up to around 477 °C.[66,67]

The TG and DSC profiles of **3** are shown in Figures 7(c) and 7(d). Upon heating **3** to 220 °C, a single exotherm is observed in the range 161-214 °C with a peak maximum at 178 °C. This exotherm is accompanied by a large weight loss amounting to 81%. We believe this thermal event results from the combination of two chemical processes: cycloaromatization of the triple bonds, which is an exothermic process occurring with no or virtually no weight loss, and decomposition of the compound, which is an exothermic process accompanied by a weight loss. In this case, decomposition probably proceeds through the breakdown of the alkylammonium groups. No melting is observed prior to this event.

A single weight loss is also observed in the TG plot of **4** (Figure 7(e)). This weight loss occurs in a large temperature range, 217-455 °C, and amounts to 88%. After that, strengthening of the carbon network occurs gradually up to 1200 °C without any noticeable step in the TG curve; at 1200 °C, a 92% weight loss is measured. When compared with the molecular weight of the starting compound, the amount of residue corresponds to the recovery of 5.6 carbon atoms. Again, this is consistent with the incorporation of all of the carbon atoms of the C≡C-C≡C unit in the final structure. By way of comparison, simple alkylammonium salts comprising bis(trifluoromethylsulfonyl)imide anions give virtually no residue upon thermolysis under a nitrogen flow.[68-72] Interestingly, however, DSC analysis shows that the thermal behavior of **4** is more complex than anticipated from TG measurements (Figure 7(f)). Compound **4** actually undergoes three thermal events in the range 20-455 °C. First, there is an endotherm in the range 88-142 °C with a peak maximum at 104 °C that corresponds to melting. These results indicate that **4** is an ionic liquid. After that, similarly to **2**, two thermal events are observed, a large exothermic phenomenon in the range 217-346 °C and an endothermic one in the range 379-455 °C. It is probable that the exothermic event is, in this case also, due to two concomitant chemical processes, cycloaromatization of the triple bonds and decomposition of the alkylammonium groups.

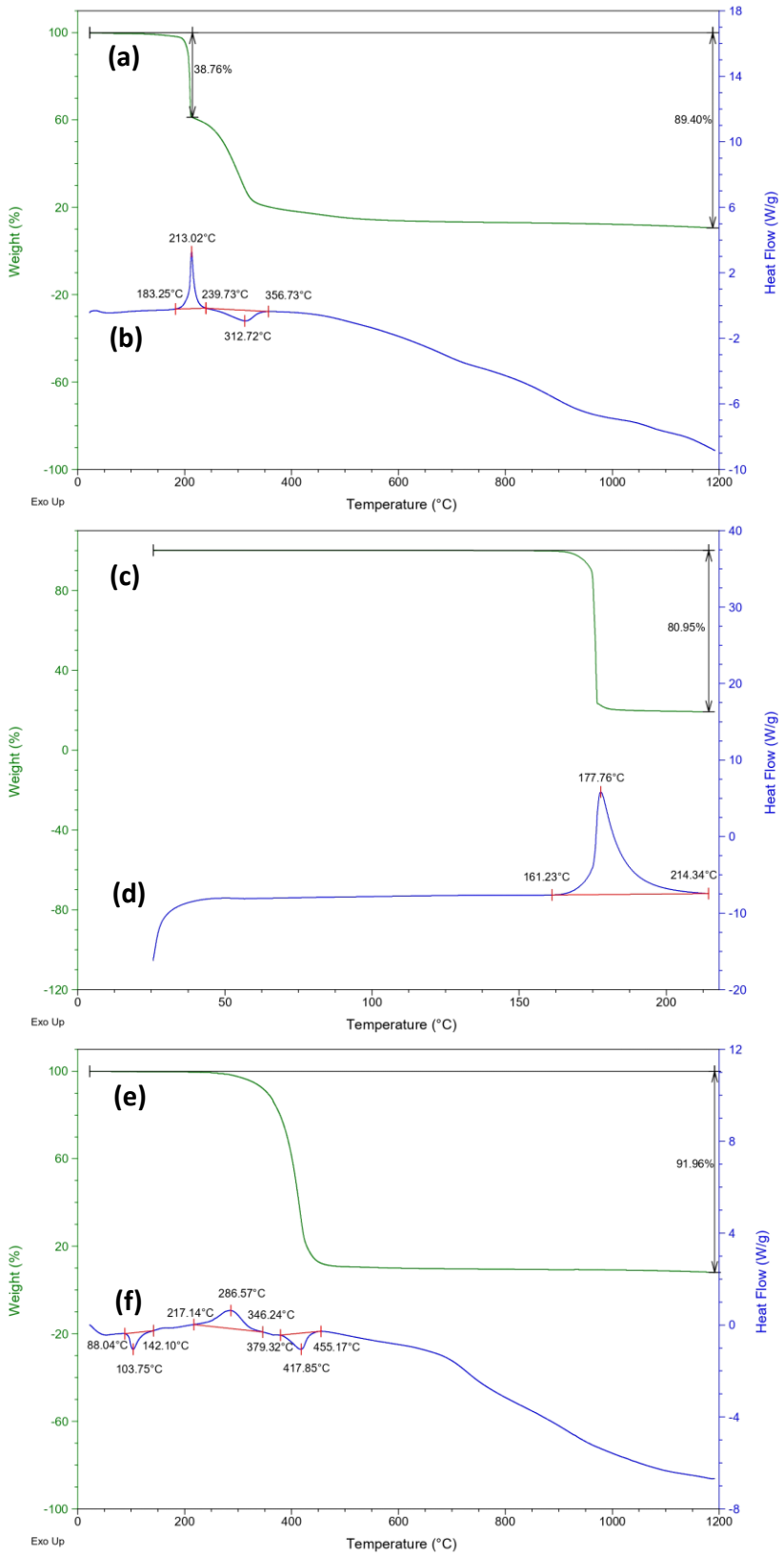

Figure 7. TG plot of **2** (a), DSC plot of **2** (b), TG plot of **3** (c), DSC plot of **3** (d), TG plot of **4** (e), DSC plot of **4** (f).

Solid-State and Molten-State Polymerization of 2-4. Although the structure-reactivity relationship established by Baughman for diacetylene polymerization is generally verified experimentally, it is worth noting that two ionic diacetylenes have been reported in the literature for which this relationship is not valid, namely 1,4-bis(4-methylpyridinium)butadiyne triflate and 1,4-bis(4-benzylpyridinium)butadiyne triflate.[24,73] Thus, the solid-state polymerization reactivities of **2-4** were assessed. Compounds **2** and **3** were heated to 110 °C for 24 hours with concomitant exposure to UV light (λ = 254 nm; light source power = 3 × 15 W), while **4** was heated to 80 °C. In none of these experiments was the formation of a polydiacetylene detected, as no $\nu_{C=C}$ band was observed in the Raman spectra in the 1500-1600 cm^{-1} range and no $\nu_{C\equiv C}$ band was identified in the 2000-2100 cm^{-1} region (see Figures 8 and S1). These observations are consistent with the crystallographic results.

The molten-state polymerization reactivity of **4** was also studied. Compound **4** was heated to 120 °C for 24 hours with simultaneous UV irradiation. Raman analysis of the resulting solid shows that the starting compound is still present and no polydiacetylene has formed (Figure 8(c)). Therefore, these results suggest that if some kind of organization exists in the liquid phase, it is not helpful for 1,4-polymerization. The same results were obtained when **4** was heated to 170 °C for a few minutes on a DSC stage (Figure 8(d)), but prolonged heating (1 h) at this temperature led to the loss of the Raman band corresponding to the triple bonds and the buildup of intense luminescence due to the formation of decomposition products (Figure 8(e)). Comparison of these observations with earlier results from our group[11] and other research teams[12-16,24,25] suggests that the reason for the lack of molten-state polymerization reactivity of **4** comes from the structure of this DA. Indeed, all of the DAs known to polymerize in the liquid state have no CH_2 group between the triple bonds and the end stoppers. Typically, however, the presence of CH_2 groups is vital when conducting solid-state diacetylene polymerization, as the stress generated in the crystal during polymerization is released by slight displacements of these latter groups. In the case of liquid-state polymerization, the presence of CH_2 moieties seems to be detrimental, as these groups surely interact *via* hydrogen bonding with nearby anions[74,75] and prevent the C≡C-C≡C rods from having the correct orientation for 1,4-polymerization. This assertion is based on the X-ray crystal structure of **4** that shows short C-H···O contacts between the CH_2 groups next to the triple bonds and oxygen atoms from $TFSI^-$ anions (*vide supra*). Recent work by Béguin and colleagues has shown that [$(CH_3CH_2)_3NH^+(TFSI^-)$], an ionic liquid structurally close to **4**, exists as an ion-pair complex in $CDCl_3$ and D_2O solvents and that, for some of the DFT

calculated structures, $CH_2\cdots O{=}S$ interactions make a significant contribution to the overall hydrogen-bonding scheme.[76] If we presume that **4** has a similar behavior and exists as an ion pair in the molten state, the C-H···O contacts observed in the solid state should be preserved. The likelihood of ion pairing is further increased by the fact that C-H···O contacts are supplemented by equally important C-H···F contacts, as pointed out in the previous discussion on the Hirshfeld surface analysis of **4**.

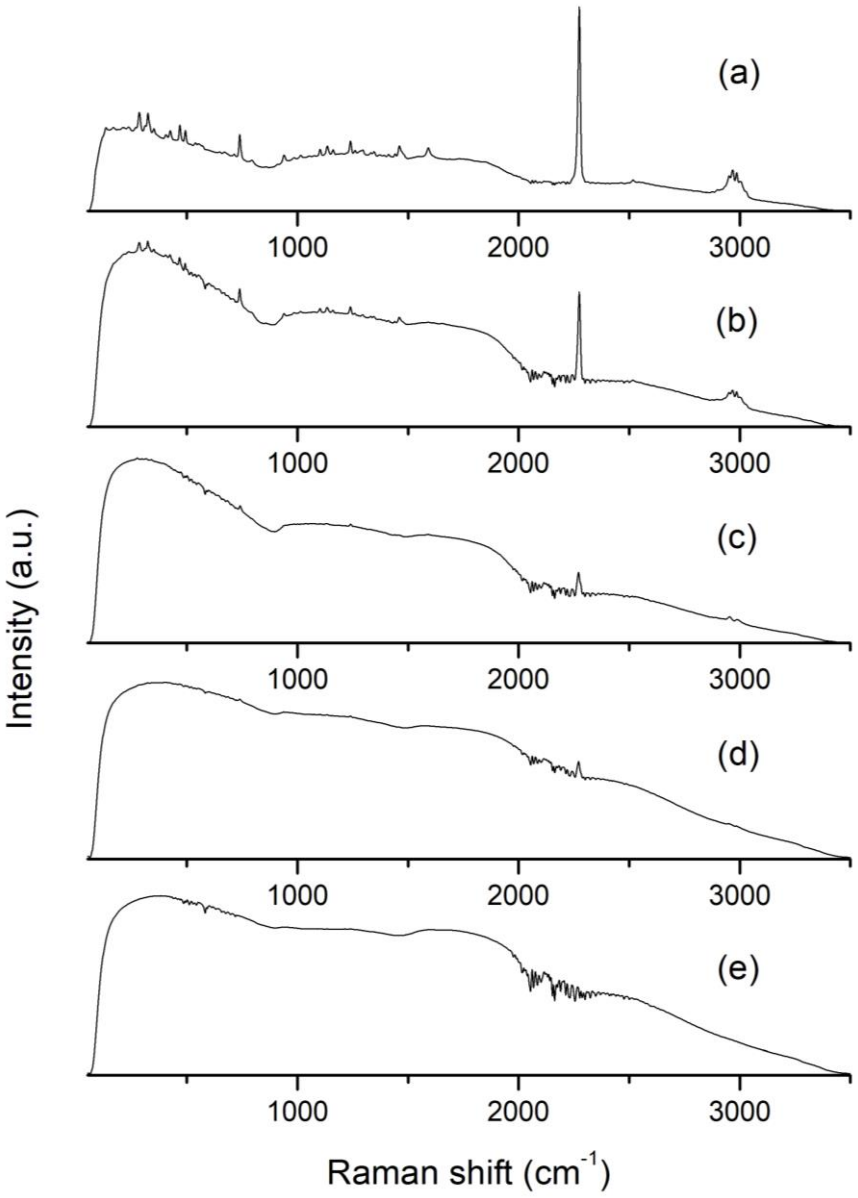

Figure 8 Raman spectra (λ_{ex} = 1064 nm) of as-synthesized **4** (a), **4** heated to 80 °C with concomitant UV irradiation (b), **4** heated to 120 °C with simultaneous UV irradiation (c), **4** heated to 170 °C on a DSC stage for a few minutes (d), and **4** heated to 170 °C on a DSC stage for 1 h (e).

Raman, XRD, HRTEM, NMR, XPS, Elemental Analysis, and Gas-Sorption Properties of the Carbon Materials Resulting from Heat Treatment of 2-4 at Various Temperatures. The Raman spectra (λ_{ex} = 785 nm) of the residues obtained after heating **2** at various temperatures are shown in Figure 9. Five thermolysis temperatures were chosen based on the previously discussed TG results, namely 220, 350, 400, 600, and 1200 °C. Regarding sample **2@220**, two large and low-intensity peaks are observed at 1336 and 1572 cm^{-1} (Figure 9(a)). The peak at 1336 cm^{-1}, commonly called the D band, is due to disorder-induced scattering from small crystallites or boundaries of larger crystallites present in graphitic materials with structural defects and is a breathing mode of A_{1g} symmetry involving phonons near the *K* zone boundary.[77-81] The intensity of this band is strictly connected to the presence of sixfold aromatic rings.[79] The D band is also observed in the Raman spectra of boron-doped highly ordered pyrolytic graphite (BHOPG), in which boron substitution decreases local lattice symmetry but does not disrupt the ordered structure.[80,82] However, this band is absent from the spectra of well-ordered defect-free graphite crystals, as the A_{1g} mode is Raman inactive because the changes in polarizability cancel over the infinite crystal.[77,79,81] The second peak at 1572 cm^{-1}, the G band, is assigned to the Raman active E_{2g} mode and is observed in all graphite-like materials.[77,79,80] It originates from bond-stretching motion of pairs of sp^2-hybridized carbon atoms and does not require the presence of sixfold rings; it occurs at all C sp^2 sites.[79] Interestingly, it has been shown that it was possible to evaluate the degree of imperfection or crystallinity of graphitic carbons by calculation of the degree of graphitization I_D/I_G.[77,79,83] In this case, the degree of graphitization is equal to 1.22 (Table 2). Furthermore, no $\nu_{C\equiv C}$ band was observed at 2263 cm^{-1} when this same sample was analyzed on a FT Raman spectrometer with λ_{ex} = 1064 nm (not shown), consistent with the complete disappearance of the starting compound. These results thus show that a temperature of 220 °C is high enough to initiate the formation of a graphitic structure, and this observation is in line with previous results obtained with other diacetylenes.[26,64]

Narrowing of the D and G bands is observed with an increase in the thermolysis temperature (Figure 9), which is suggestive of a better crystallinity of the samples due to a decrease in the amounts of defects and/or an increase in the size of the graphitic domains.[77,78,83-86] Also, it is remarkable to note that the degree of graphitization of the materials increases with increasing thermolysis temperature and reaches 2.37 at 1200 °C (Table 2). As the intensity of the D band is strictly connected to the presence of sixfold

aromatic rings (see above), such a variation suggests that we are monitoring the formation of six-membered aromatic rings by cyclotrimetrization of the triple bonds of the starting diacetylene.[11,26,64,65,87,88] Also, the size of the graphitic domains is expected to augment with increasing thermolysis temperature.[85,89] So, if we refer to Figure 5 displayed in Ferrari's 2000 report,[79] the fact that the degree of graphitization increases with in-plane crystallite size, L_a, suggests that the graphitic domains have sizes below 2 nm. Quite interestingly, by using the Tuinstra-Koening relation $I_D/I_G = 4.4/L_a(\text{nm})$,[77] a L_a value of 1.86 nm is calculated for **2@1200**. For crystallite sizes larger than 7 nm, another band located at 1620 cm^{-1}, the D' band, starts separating from the G band; this band was not observed for the present samples.[78,79,83,86]

As shown in Table 2, the positions of the D and G bands of the carbon residues remain unchanged up to about 400 °C, which corresponds roughly to the end of the weight loss in the TG curve. For **2@600**, a small redshift of the D band to 1331 cm^{-1} is noticed, and, for **2@1200**, a significant redshift to 1306 cm^{-1} is detected. A similar situation has been observed previously with graphite-like materials prepared from diacetylenes, [26,64] and it has been suggested that this was due to a decrease in the nitrogen contents of the residues.[86,90] Curiously, however, the G band moves in the opposite direction and is observed at 1594 cm^{-1} for the sample prepared at 1200 °C. It is quite likely that the decrease in the nitrogen contents contributes to this blueshift,[87,88] but, more broadly, Ferrari[79] and Merlen[83] point out that the position of the G band is influenced by the state of disorder in the material, notably clustering of the sp^2 phase, bond disorder, presence of sp^2 rings and/or chains, presence of sp^3 carbons, etc., and that values in the 1590-1600 cm^{-1} range are typical of nanocrystalline graphite. Based on the amorphization trajectory shown in Figure 7 of Ferrari's 2000 article,[79] **2@1200** lies probably near the upper-left corner of the Stage 2 domain, *i.e.* the region where the nanocrystalline graphite to *a*-C transformation takes place. Heating **2@1200** to much higher temperatures should yield less disordered graphitic samples showing a G band position closer to the accepted value of 1582 cm^{-1}.[84]

Raman data for **3@220** are shown in Figure S2(a). Similarly to **2@220**, the spectrum shows two large and low-intensity peaks at 1344 cm^{-1} (D band) and 1573 cm^{-1} (G band), suggestive of the presence of graphite-like domains. The degree of graphitization, 1.17, is similar to that of **2@220** (1.22).

Thermolysis of **4** was carried out at 373, 475, 600, and 1200 °C. Interestingly, the residue obtained at 373 °C is actually not a solid but a gummy material. Its Raman spectrum

(Figure S2(b)) shows no identifiable peak in the 1000-2000 cm^{-1} region. The Raman spectrum of the residue prepared at 475 °C is shown in Figure S2(c). It shows two major peaks at 1337 cm^{-1} and 1585 cm^{-1} corresponding respectively to the D and G bands of a graphitic material structurally similar to those discussed previously. Also, the spectrum exhibits two ill-defined peaks at 1247 cm^{-1} and 1454 cm^{-1} which were not detected in the spectra of the previous samples. As already noticed for compound **2**, the 1337 cm^{-1} band of **4@475** undergoes a redshift with an increase in the thermolysis temperature, and the 1585 cm^{-1} band undergoes a blueshift. These bands are observed at 1311 and 1606 cm^{-1} for **4@1200** (Figure S2(e)). The additional bands at 1247 and 1454 cm^{-1} are not clearly visible in the spectrum of **4@600** (Figure S2(d)), but they evidently contribute to the large linewidths of the peaks at 1332 and 1587 cm^{-1}. Yet, owing to the narrowing of the Raman lines with increasing thermolysis temperature, these additional bands show up again in the spectrum of **4@1200**; their new positions are 1197 and 1486 cm^{-1}, respectively. These extra bands appear to be inter-related: similarly to the D and G bands of the main graphitic phase, the 1247 cm^{-1} line undergoes a redshift with increasing thermolysis temperature, and the 1454 cm^{-1} line a blueshift. Thus, it looks as if a second kind of graphitic material might be involved, but further evidence is needed. Certainly, this second graphitic phase cannot be graphite oxide, as the D and G bands of this material are observed around 1350 and 1600 cm^{-1}.[91] Yet, as sulfur is found to be present in **4@1200** by XPS analysis (Table 3), it is possible that the 1454 cm^{-1} line might originate from sulfur-doped graphite. Indeed, an extra band of unknown origin was observed at 1436 cm^{-1} in the Raman spectra of CVD-grown few-layer graphene samples heat-treated at 500 °C with sulfur vapor.[92] On the other hand, XPS analysis indicates that **4@1200** also contains some fluorine (Table 3), so it is possible that some sort of fluorinated graphitic phase might be present as well. Indeed, it is known that the frequencies of the D and G Raman bands of graphite are very much affected by fluorination due to a weakening of the C-C bond.[93] In this connection, a band was observed at 1444 cm^{-1} in the Raman spectrum of stage 2 graphite fluorine intercalation compounds, which was attributed to Brillouin zone folding due to intercalation with fluorine.[94] Also, an extra band was detected at 1453 cm^{-1} in the Raman spectrum of fluorine-intercalated graphite fibers, and this band was speculated to arise from considerable lattice disorder caused by the strong interaction of fluorine with the host material.[95] Last, a band was observed at 1476 cm^{-1} in the Raman spectrum of an intercalated compound of graphite fluoride with *n*-heptane, and it was suggested that this band was due to disorder induced by attachment of fluorine atoms to the graphitic network.[96] So, extra bands

similar to the 1454 cm^{-1} line of **4@1200** have been observed before for fluorine-doped graphite samples, but the origin of this band is unclear. Interestingly, however, no mention was made in all of these studies of an additional band around 1200 cm^{-1}. Concerning this latter band, another scenario could be that it originates from trifluoromethylation of the graphitic material, as the ν_{as} and $\nu_s(CF_3)$ lines of solid LiTFSI appear in the 1200-1250 cm^{-1} region.[97,98] XPS measurements seem to agree with that possibility, as a peak is observed at 688.9 eV that is assigned to CF_3 groups (Table 3). Yet, it is also noteworthy that a combination of five bands had to be used to achieve accurate curve fitting of the first-order Raman spectra of soot samples.[99] Amongst these bands, one band, the D4 band, has a Raman shift of about 1200 cm^{-1}. Several assignments have been put forth for this band such as graphitic lattice disorder (A_{1g} symmetry), formation of polyene-like structures, or presence of ionic impurities.

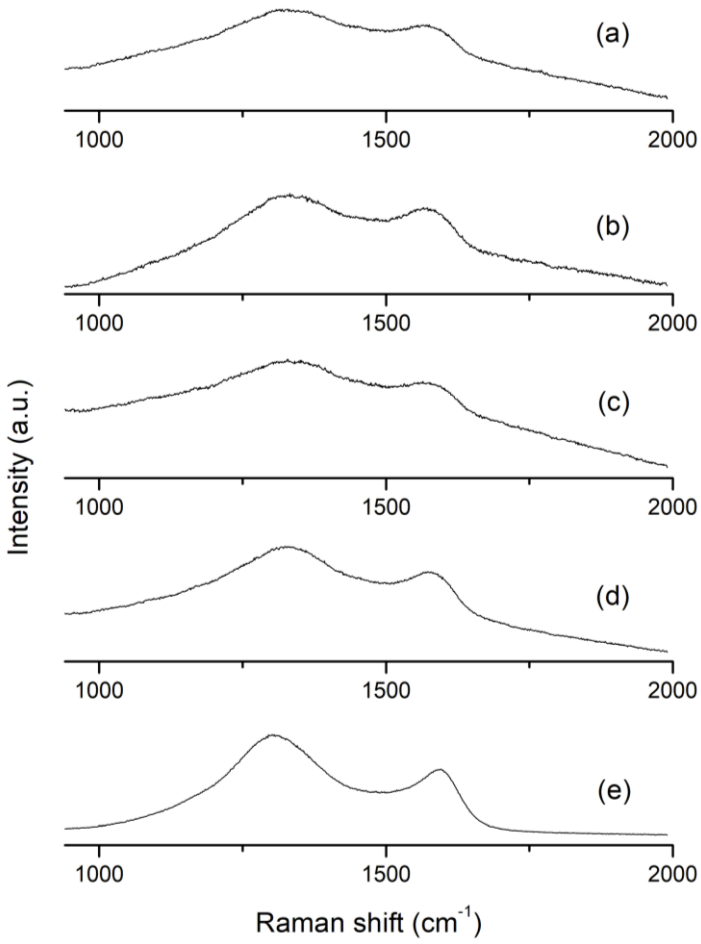

Figure 9 Raman spectra (λ_{ex} = 785 nm) of the residues obtained after thermolysis of **2** at the following temperatures: 220 °C (a), 350 °C (b), 400 °C (c), 600 °C (d), 1200 °C (e).

The carbon residues were also characterized by elemental analysis. For compound **2**, it is found that the N and H contents decrease with increasing thermolysis temperature to reach respectively 1.75 and 1.08 wt % at 1200 °C (Table 2). The N content is much lower than those measured upon thermolysis of 1,6-bis(3-methylimidazolium)hexa-2,4-diyne dibromide and 1,6-bis(3-methylbenzimidazolium)hexa-2,4-diyne dibromide at 1100 °C, namely 4.4 and 4.6 wt %.[26] We believe this is due to two joint factors: first, the thermolysis temperature is one hundred degrees higher in the present study than in the previous one.[26,31,38] Second, since alkyl substituents decompose more readily than aromatic groups, nitrogen loss is expected to be easier when this element belongs to an alkylammonium group than when it is part of an heteroaromatic moiety. Furthermore, XPS analysis of **2@1200** indicates that there is no iodine left in the sample (Table 3). Presumably, iodine is lost during thermolysis through a Hofmann-type elimination reaction or a reverse Menshutkin reaction.[26] Compound **4** behaves similarly to **2**. At 475 °C, the N and H contents of the residue are respectively 2.39 and 3.34 wt % (Table 2), and these amounts drop drastically to 1.40 and 0.42 wt % at 1200 °C. As the N drop parallels the H drop, and since H atoms are present only in alkyl fragments, we believe these drops are due to the decomposition of residual alkylammonium groups. The S and F contents of **4@1200** were also determined. XPS measurements show that both elements are present in the sample. Three types of environments are found for sulfur, C-S-C, S-O, and C-SO_x-C (x = 2, 3),[92,100-106] and two kinds of environments are detected for fluorine, semi-ionic C-F and CF_3.[104,107-110] Thus, the present work shows that carbonization of ionic diacetylenes may be an alternative method to introduce doping elements in a graphite structure.[111]

The X-ray powder patterns of the residues resulting from thermolysis of **2** at various temperatures are shown in Figure 10. These diffractograms are in keeping with the aforementioned Raman data. In particular, the diffractogram of **2@220** shows the presence of a broad line at $2\theta \approx 25°$ that corresponds to the (002) plane of a graphitic structure.[112,113] Also, as previously observed for the Raman peaks, the diffractions peaks become narrower with increasing thermolysis temperature, which suggests an increase in the crystallinity of the samples. At 600 °C, a second broad peak is visible at $2\theta \approx 44°$ that corresponds to the (10) asymmetric line of graphitic domains with larger sizes.[112,113]

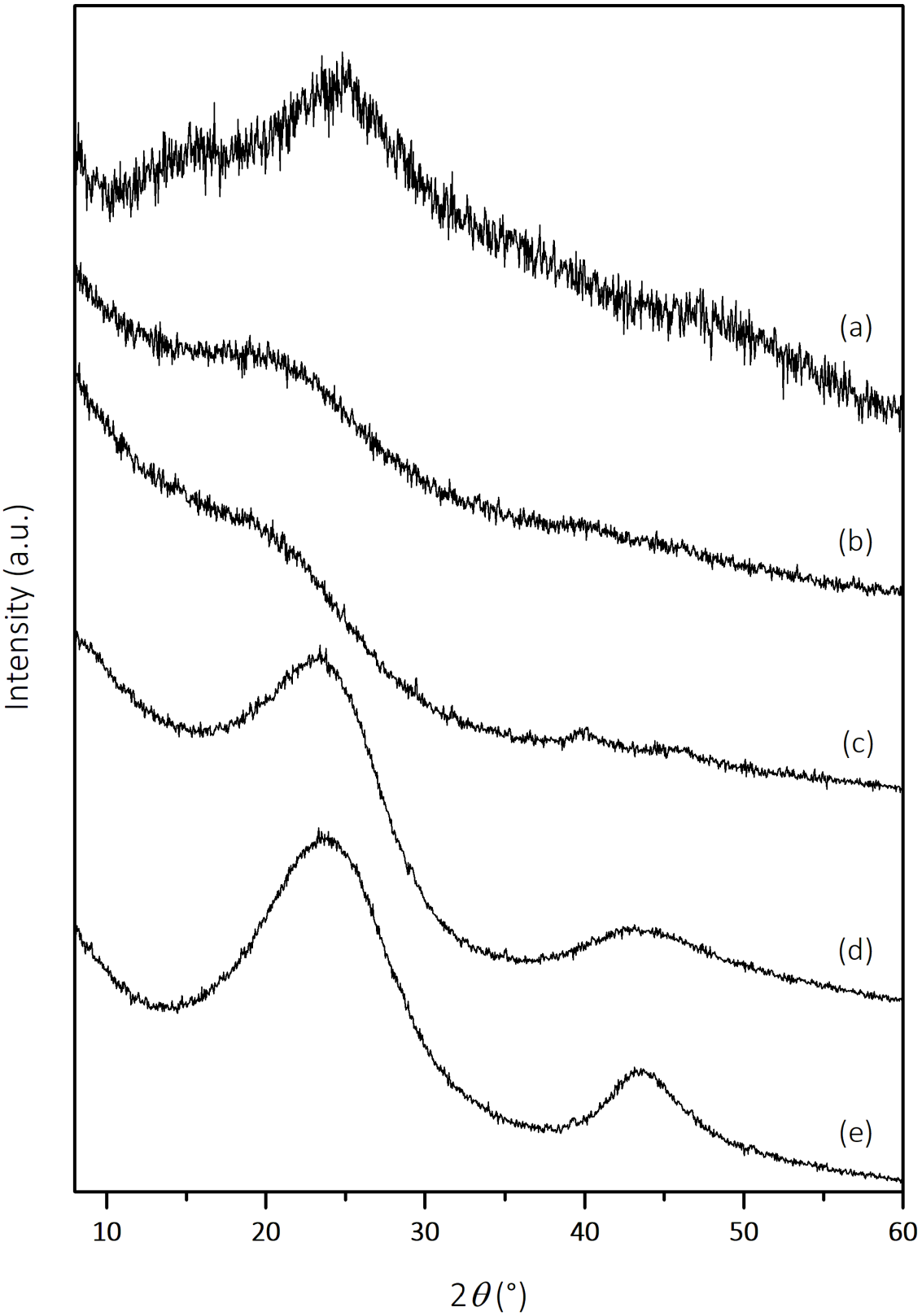

Figure 10 X-ray powder patterns of the residues obtained after thermolysis of **2** at the following temperatures: 220 °C (a), 350 °C (b), 400 °C (c), 600 °C (d), 1200 °C (e).

From the diffractograms shown in Figure 10 it is possible to extract three important parameters describing the 3D organization of graphite-like materials: the mean distance between graphene sheets as given by the $d_{(002)}$ spacing, the coherently scattering domain size along the *c* axis L_c , and the in-plane crystallite size L_a. The diffraction peaks were fitted with the WinPLOTR program[114] using pseudo-Voigt functions adapted with asymmetry parameters when necessary. From the full width at half maximum (FWHM) of the fitted peaks, L_c and L_a were calculated using the Scherrer equation, following the methodology developed by Puech *et al.*[113] A Scherrer factor of 0.9 was used for the (002) peak, and a factor of 1.84 for the (10) peak. For **2@220**, these parameters could not be estimated, as the diffraction peaks do not show sufficient resolution, and, for **2@350** and **2@400**, only $d_{(002)}$ and L_c could be determined. Table 2 indicates that $d_{(002)}$ decreases with increasing thermolysis temperature, meaning that the graphene planes are getting closer. The value measured for **2@1200**, 3.73 Å, is still quite far from the value measured for perfect graphite samples, 3.36 Å, but is in line with the values reported in previous studies on diacetylenes.[26,64] L_c shows no significant change with increasing thermolysis temperature and remains stable at about 10 Å. Presumably, the temperatures used in this study are not high enough to induce large variations of L_c. In the case of pyrolytic carbon and coal-tar pitch, an annealing temperature of about 1400 °C is necessary to produce marked changes in L_c.[113] Paradoxically, L_a is a lot more sensitive to the thermolysis temperature and increases from 15 to 27 Å on passing from 600 to 1200 °C. Thus, ordering of the graphitic structure appears to be anisotropic and occurs mainly in the *ab* plane at moderately high temperatures. The way the crystalline domains grow is certainly linked to the 2D nature of graphite: an increase in the size of the crystalline domains in the *ab* plane necessitates the growth and ordering of the graphene sheets *via* chemical reactions. Along *c*, an increase in the size of the crystalline domains requires the assembly of the graphene sheets *via* weak noncovalent interactions. Last, the value of L_a found for **2@1200**, 27 Å, is of the same order of magnitude as that found by Raman spectroscopy, 18.6 Å (*vide supra*).

The diffractogram of **3@220** (Figure S3(a)) exhibits an ill-defined line at $2\theta \approx 24°$ that reveals the presence of an emerging graphitic phase, in accord with the Raman data. The diffractogram of **4@475** (Figure S3(b)) consists of a single well-resolved (002) line, and the (10) asymmetric line of graphitic domains becomes visible in the diffractogram of **4@600** (Figure S3(c)). As a result, $d_{(002)}$, L_c, and L_a were calculated for **4@600** and **4@1200**, but only the first two parameters could be derived for **4@475**. The values are given in Table 2. Except for **4@1200**, the $d_{(002)}$ values found for carbonized **4** are slightly smaller than those measured

for thermolyzed **2**, suggesting a higher degree of interlayer organization. With regard to L_c, this parameter decreases with increasing thermolysis temperature and reaches a value at 1200 °C that is similar to that measured for **2@1200**. Such a variation is surprising, as the opposite trend is observed upon annealing pyrolytic carbon and coal-tar pitch at temperatures beyond 1000 °C.[113] It is unclear whether this situation comes from the fact that **4** is in the molten state when decomposition starts. On the other hand, L_a increases with increasing thermolysis temperature and reaches a value at 1200 °C that is close to that of **2@1200**.

Residues **2@1200** and **4@1200** have been characterized by HRTEM. Figures 11(a) and 11(b) show the corresponding micrographs. Basically, both solids seem to be made of two kinds of domains that are interwoven, one kind with an orange peel texture that certainly corresponds to amorphous carbon, and a second kind corresponding to graphitic domains where worm-like aggregates are visible. These observations are fully consistent with the poor crystallinity of the samples and suggest the presence of turbostratic carbon. According to Oberlin, these carbon materials are at stage 2 of the graphitization process, which totals four stages.[115,116] Occasionally, it is also possible to distinguish well-organized graphitic domains in which graphene planes assemble in a perfectly parallel fashion. These domains are outlined by red rectangles in Figures 11(a) and 11(b). A line profile analysis of these domains was carried out. For **2@1200**, a distance of 0.367 nm was measured between neighboring layers (Figure 11(c)), and, for **4@1200**, a value of 0.368 nm was found (Figure 11(d)). These figures compare well with the mean values determined by XRD, *i.e.* 0.373 and 0.380 nm.

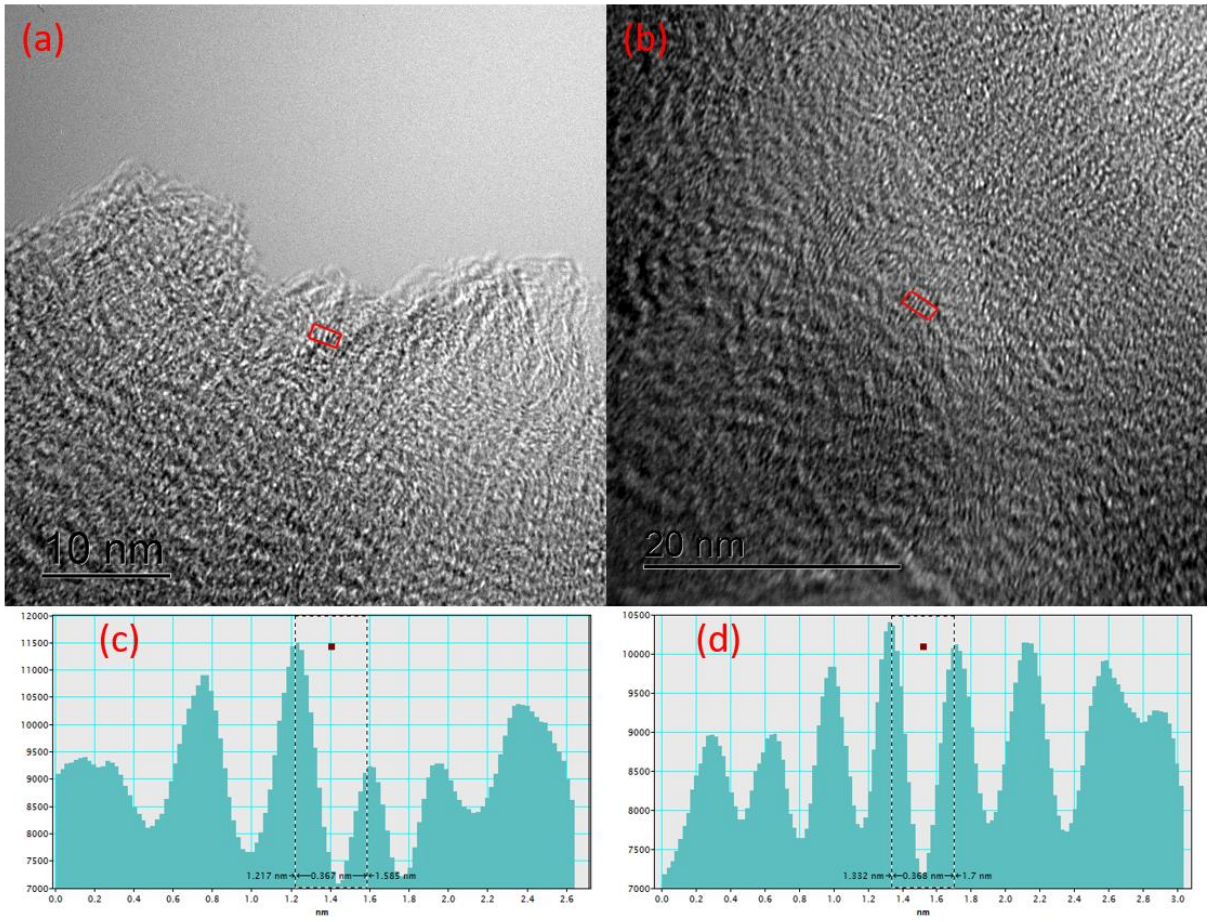

Figure 11. HRTEM micrographs of **2@1200** (a) and **4@1200** (b). In each micrograph, a line profile analysis of one well-defined graphitic domain (outlined by a red rectangle) has been carried out, and the corresponding results are shown in (c) (**2@1200**) and (d) (**4@1200**).

The solid-state ^{13}C NMR spectrum of **2@220** is shown in Figure 12(d). It shows several peaks at $\delta \approx 10$ and 50 ppm assigned to residual methyl and methylene groups. However, sharp signals are no longer visible at $\delta = 69.8$ and 76.3 ppm, suggesting the disappearance of the acetylenic carbons of the precursor (Figure 12(c)). These peaks have been replaced by a broad hump at $\delta \approx 130$ ppm that corresponds to aromatic carbons. At least two major types of aromatic carbons are present in the sample, as the hump is made of two components. The aromatic rings originate from cyclotrimerization of the acetylenic carbons of the precursor, as previously observed with other diacetylenes.[26,64,65] The solid-state ^{1}H NMR spectrum of **2@220** is shown in Figure 12(b). The detection of signals at $\delta = 1.33$ and 3.21 ppm confirms the presence of methyl and methylene groups, and an additional peak is observed at $\delta = 8.08$ ppm that corresponds to aromatic protons.

The solid-state ^{13}C NMR spectrum of **3@220** is shown in Figure S4(d). It shows a broad peak at $\delta \approx 12$ ppm that originates from residual methyl groups, and signals due to methylene groups are certainly buried underneath the spinning sideband at $\delta \approx 45$ ppm. Sharp signals due to the acetylenic carbons of the precursor (Figure S4(c)) are no longer visible at δ = 69.7, 70.9, 73.7, and 74.0 ppm. These peaks have been replaced by a broad hump at $\delta \approx 125$ ppm indicative of the formation of polyaromatic structures. The solid-state ^{1}H NMR spectrum of **3@220** is shown in Figure S4(b). Signals are detected at δ = 1.22 and 3.15 ppm that confirm the presence of methyl and methylene groups, and a broad peak is observed at δ = 7.10 ppm that corresponds to aromatic protons.

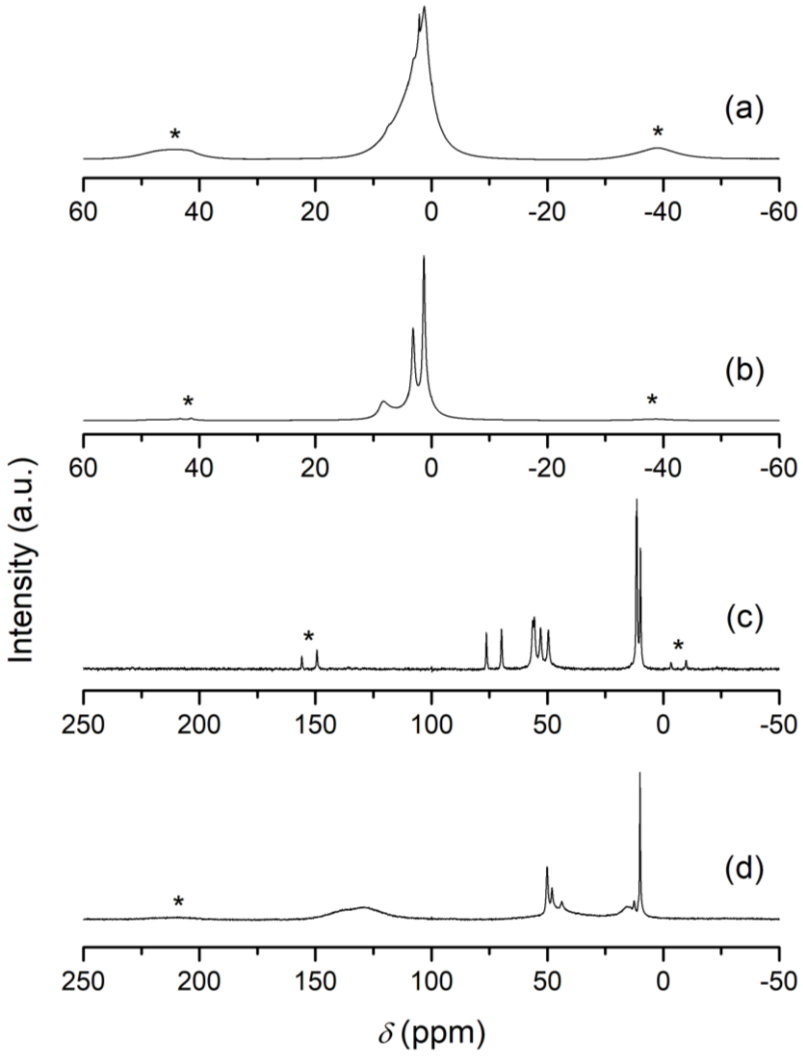

Figure 12. Solid-state ^{1}H and ^{13}C NMR spectra of **2** ((a) and (c)) and **2@220** ((b) and (d)). Peaks marked with an asterisk are spinning sidebands. In spectrum (d), the right-hand side spinning sideband overlaps with the resonance signals at $\delta \approx 50$ ppm.

Residue **4@373** was chosen for NMR characterization because it is obtained right after the first exotherm. Yet, since it is a gummy material, its characterization had to be done in solution. The ^{1}H and ^{13}C NMR spectra of **4@373** in CD_2Cl_2 solvent are shown in Figures S5(b) and S5(d). As previously noted for **2** and **3**, the ^{13}C NMR spectrum reveals the disappearance of the acetylenic carbons of **4** (δ = 67.9 and 72.9 ppm in Figure S5(c)) and the growth of numerous signals in the 125-150 ppm region corresponding to aromatic carbons. The ^{1}H NMR spectrum of **4@373** shows the vanishing of the CH_2 groups adjacent to the triple bonds (δ = 4.17 ppm in Figure S5(a)) and the growth of numerous peaks beyond 6.5 ppm due to aromatic protons.

The gas sorption properties of **2@1200** and **4@1200** were evaluated. Figure 13(a) shows the N_2 sorption isotherms at −196 °C of **2@1200**. The adsorption branch exhibits a typical type I isotherm with a rapid increase at low pressure promptly followed by a plateau; the maximum adsorption capacity is reached at a relative pressure p/p° of about 0.1. This kind of isotherm is characteristic of microporous solids. Also, the fact that no hysteresis is observed in Figure 13(a) suggests the absence of mesopores. Furthermore, a rapid increase is observed at high pressure ($p/p° \approx 1$) that suggests the presence of small macropores that probably correspond to inter-aggregate regions. This last result indicates the presence of particles with relatively small sizes. As given in Table 4, the BET surface area of **2@1200** is 88 $m^2\ g^{-1}$ and the micropore surface 82 $m^2\ g^{-1}$. The total volume of pores is estimated at 21 $cm^3\ g^{-1}$ STP and, in accord with the type I character of the isotherm, micropores represent the majority of the volume with 20 $cm^3\ g^{-1}$ STP.

DFT methods were used to simulate the N_2 sorption isotherms of **2@1200**, and the most appropriate model that was found is the one that uses a distribution of slit-shaped pores on a carbon surface showing some heterogeneities. The resulting distribution (Figure 14(a)) not only confirms the microporous nature of the sample but reveals also the ultra-microporosity of the latter, as the majority of the adsorbed volume is located in pores with sizes smaller than 1 nm.

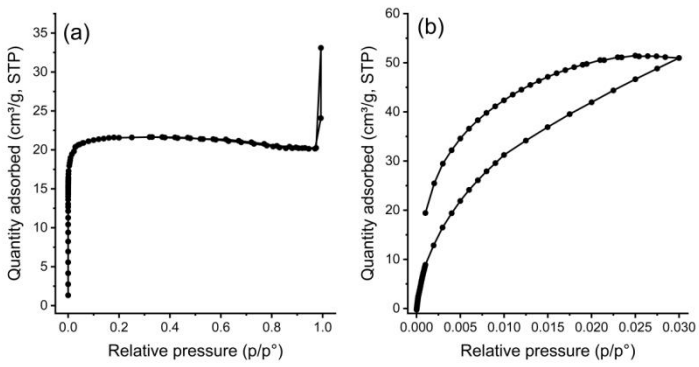

Figure 13. N_2 sorption isotherms at −196 °C (a) and CO_2 sorption isotherms at 0 °C (b) of **2@1200**.

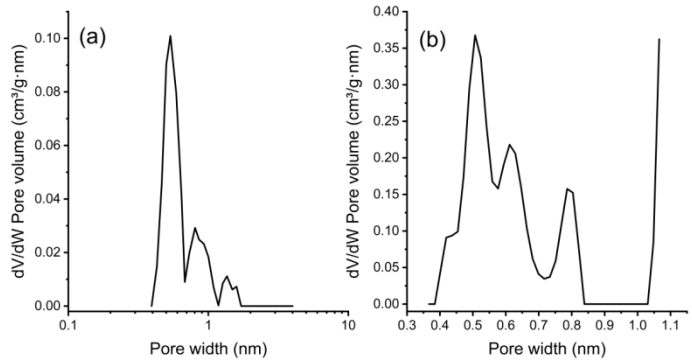

Figure 14. Pore size distributions of **2@1200** as obtained by DFT analysis of the N_2 sorption isotherms at −196 °C (a) and CO_2 sorption isotherms at 0 °C (b).

The ultra-microporosity of **2@1200** was verified by measuring the CO_2 adsorption-desorption isotherms at 0 °C, a technique that is dedicated to the analysis of the microporous solids. In this case, an hysteresis is observed that reflects the difficult diffusion of the gas molecules during desorption (Figure 13(b)). Such a behavior indicates the presence of relatively clogged ultra-micropores ("bottle-shaped" pores).[117] Analysis of this isotherm using the BET theory furnishes the data listed in Table 4. Remarkably, the calculated surface area is quite high, 321 $m^2\ g^{-1}$. A pore size distribution was established by means of DFT methods. In this case, the best fitting model consists of a slit-shaped geometry with a generic surface instead of a carbon surface. This requirement reveals a marked difference as compared with a pure carbon surface, certainly because of the presence of heteroatoms. The resulting distribution (Figure 14(b)) shows a series of fairly well structured pores with apertures of the

following dimensions: 0.42, 0.51, 0.62, and 0.79 nm. The relative contributions of these pores to the total adsorbed volume are respectively 8.8, 46.7, 29.2, and 15.2 %.

These results are quite remarkable, as they differ significantly from those obtained previously for carbon residues prepared at 1100 °C from imidazolium- and benzimidazolium-appended diacetylenes. Specifically, for these latter materials, very low BET specific surface areas in the range 0.36-3.43 $m^2\ g^{-1}$ were measured.[26] We believe this dichotomy originates from the large size of the dication used in the present study. Indeed, earlier work by Dai and colleagues has demonstrated the templating role of organic cations during micropore generation, building on the observation that carbonaceous materials derived from ILs containing bulky cations had high surface areas.[36]

The N_2 sorption isotherms at −196 °C of **4@1200** are shown in Figure S6(a). In this case, the shapes of the isotherms are quite different from those of **2@1200**: a linear increase in the adsorbed gas volume with increasing p/p° is observed. Nonetheless, the adsorbed volume at p/p° = 1, about 24 $cm^3\ g^{-1}$ STP, is similar to that of **2@1200** at the same pressure, around 21 $cm^3\ g^{-1}$ STP. Such a type II isotherm without hysteresis is characteristic of a macroporous or a nonporous solid. Analysis of these isotherms using the BET theory and application of the *t*-plot method gives a surface area of 33 $m^2\ g^{-1}$ (Table 4); the micropore surface and volume cannot be obtained by the *t*-plot model because there not enough data points to draw a tangent line. Yet, these findings must be tempered. Close inspection of the isotherm of **4@1200** (Figure S6(a)) shows a slight but sharp deflection at low pressure indicative of the presence of a small amount of micropores. The presence of micropores is confirmed by DFT methods that give a micropore volume of about 12 % of the total volume. Furthermore, while **2@1200** showed a uniform slit-shaped porosity, a composite geometry had to be used for **4@1200** to fit correctly the adsorption-desorption isotherms and obtain the pore size distribution shown in Figure S7(a). The micropores seem to adopt a cylindrical shape whereas the mesopores maintain a slit-shaped geometry. The organization of the mesopores is centered around two major sizes, 3 and 5 nm. They constitute the majority of the porosity and account for 88 % of the volume.

These observations clearly show that **2@1200** and **4@1200** have quite different microstructures and suggest the involvement of the anion in the formation of the carbon material. Among the many possible reasons for this dichotomy, the size difference between the iodide and the $TFSI^-$ anion is the most obvious one. Also, as no iodine is detected by XPS in **2@1200**, it is possible that I^- may serve as a porogen during the thermal treatment. Last,

4@1200 contains small amounts of fluorine and sulfur that could induce the formation of a larger quantity of heterogeneities on the surface. In this connection, detailed analysis of the BET results shows an interesting difference between **2@1200** and **4@1200**. The C_{BET} constant differs significantly between the two materials, *i.e.* 1446 for **2@1200** and 14 for **4@1200**. This parameter is known to be directly proportional to the energy of adsorption of the gas probe molecules on the surface. This difference suggests a reduced polarity of the **4@1200** surface against the quadrupole moment of N_2 (presence of fewer active sites), as opposed to the **2@1200** surface.

The CO_2 sorption isotherms at 0 °C of **4@1200** are shown in Figure S6(b). These isotherms are similar to those of **2@1200**, except for the fact that the volume of adsorbed gas is much smaller. This last point is an additional proof of the presence of small amounts of micropores and ultra-micropores in **4@1200**. The CO_2 sorption isotherms were analyzed by means of DFT methods to get a pore size distribution (Figure S7(b)). Remarkably, the calculated distribution looks very similar to that of **2@1200**, notwithstanding the scale factor. It shows a series of fairly well structured pores with apertures of the following dimensions: 0.54, 0.61, 0.68, and 0.80 nm.

Analysis of the CO_2 sorption isotherms at 0 °C of **2@1200** and **4@1200** using the Dubinin-Astakhov equation[118] allows calculation of the S_{DA} and V_{DA} values as given in Table 4. Gratifyingly, these values are close to those obtained with the BET method (the Dubinin-Astakhov model is recognized as an empirical but effective model to characterize microporous carbon materials). Interestingly also, when using the Dubinin-Astakhov equation, it is found that different values of the *n* exponent have to be used for the two samples, 2.10 for **2@1200** and 1.58 for **4@1200**. This parameter is directly linked to the heterogeneity of the carbon surface: the higher the *n* value, the more homogeneous the micropores are (in terms of energy of adsorption and hence in terms of pore size distribution). So, the microporous surface of **4@1200** is definitely more heterogeneous than that of **2@1200**, as already surmised from the N_2 sorption results discussed above. Furthermore, analysis of the CO_2 sorption data with the BET model gives similar C_{BET} constants for **2@1200** and **4@1200**, 72 and 21, respectively.

In conclusion, combination of the gas-sorption results of **2@1200** and **4@1200** with the XPS data reveals the influence of the I^- and $TFSI^-$ anions on the microstructure of the final carbon material. The smallest I^- anion serves as a porogen, leads to a large microporosity, and is consumed during the heat treatment. Conversely, the bulky $TFSI^-$ anion

is partly maintained in the carbon matrix, in the microporosity possibly, and leads to a heterogeneous and cluttered ultra-microporosity (the slits are partially occupied and tend towards a more cylindrical geometry).

CONCLUSION

Three symmetrical diacetylenes bearing tetraalkylammonium substituents have been prepared starting from 1,6-bis(diethylamino)hexa-2,4-diyne (**1**), namely 1,6-bis(triethylammonium)hexa-2,4-diyne diiodide (**2**), dinitrate (**3**), and bis[bis(trifluoromethylsulfonyl)imide] (**4**). The organization of these salts in the solid state has been investigated by single-crystal X-ray diffraction methods. As previously noted for other ionic diacetylenes, salts **2**-**4** self-assemble in stacks. These stacks are held in place by numerous C-H···X (X = N, O, F, I) interactions with nearby anions, and, in the case of **2**, C-H···π interactions between neighboring DA cations are also observed. Due to the bulkiness of the end-groups, the distance between two successive C≡C-C≡C units in a stack is large, *e.g.* 6.819 Å for **2**, and structural results indicate that this distance becomes larger as the size of anion increases. Hence, it is unsurprising to find that DAs **2**-**4** do not undergo topochemical polymerization.

Salts **2** and **3** do not have a melting point, yet association of the $TFSI^-$ anion with the 1,6-bis(triethylammonium)hexa-2,4-diyne cation gives a low-melting solid, **4**, that is actually an ionic liquid. As far as we know, compound **4** is the first diacetylenic ionic liquid ever reported. Compound **4** is stable in the liquid state at 120 °C for several hours and remains unchanged at 170 °C for a few minutes without any sign of PDA formation, which signifies that if some kind of organization exists in the liquid phase, it is not helpful for 1,4-polymerization. Compound **4** probably exists as an ion pair in the molten state due to numerous C-H···O and C-H···F contacts between the cation and the anion, thus preventing the C≡C-C≡C rods from approaching each other. But, also, the steric demand of the tetraalkylammonium substituents certainly contributes to making molten-state polymerization more difficult.

Ionic DAs **2**-**4** can be used as precursors for the preparation of nitrogen-doped carbon materials. This is in sharp contrast with simple alkylammonium salts comprising iodide and bis(trifluoromethylsulfonyl)imide anions, for which no or virtually no residue is recovered upon thermolysis under a nitrogen flow. The first step in the construction of the graphite-like structures is cycloaromatization of the triple bonds occurring at temperatures close to 200 °C. The formation of intermediate phases such as enyne, butatriene, or polyene structures with dangling alkynyl groups is not observed, as ascertained from NMR and Raman spectroscopic analyses.

The carbon yields are low because the precursors consist almost exclusively of alkyl groups, so, in that respect, the use of heteroaromatic substituents is clearly an asset. However, we were agreeably surprised to discover that **2@1200** and **4@1200** exhibited nitrogen contents of 1.75 and 1.40 wt%, respectively, which is not bad considering the high thermolysis temperature used. But the most significant achievement concerns the BET specific surface area: very low BET surface areas in the range of 0.36 to 3.43 $m^2\ g^{-1}$ have been measured in previous work for carbon residues prepared by thermolysis of imidazolium- and benzimidazolium-appended diacetylenes at 1100 °C. Here, the BET specific surface area of **2@1200** derived from dinitrogen sorption experiments is 88 $m^2\ g^{-1}$ and that of **4@1200** 33 $m^2\ g^{-1}$. These results highlight the pivotal influence of the size of the cation on the microstructure of the resulting carbon material. In addition, **2@1200** appears to be mostly microporous and **4@1200** mesoporous, which shows that the anion is equally important in the structuring of the final solid: its size is surely decisive, but its incorporation in the carbon matrix, in whole or in part, is certainly crucial as well. Indeed, XPS analysis of **4@1200** indicates that, besides nitrogen, small amounts of fluorine and sulfur are included in the material. Consequently, carbonization of ionic diacetylenes can be regarded as an alternative method to introduce doping elements in a graphite structure. We intend to investigate this issue further by calcining new diacetylenic precursors equipped with anions containing other heteroelements. Also, these newly synthesized carbon materials along with the ones prepared in the present study will be tested as anodes for lithium-ion batteries.

ASSOCIATED CONTENT

Supporting Information

The Supporting Information is available free of charge at https://pubs.acs.org/doi/10.1021/acs.cgd.xxxxxxx.

Figure S1: Raman spectra (λ_{ex} = 1064 nm) of as-synthesized **2**, **2** heated to 110 °C with concomitant UV irradiation, as-synthesized **3**, and **3** heated to 110 °C with simultaneous UV irradiation; Figure S2: Raman spectra (λ_{ex} = 785 nm) of the carbonaceous material resulting from pyrolysis of **3** at 220 °C and of the residues obtained after thermolysis of **4** at the following temperatures: 373 °C, 475 °C, 600 °C, 1200 °C; Figure S3: X-ray powder patterns of the carbonaceous material resulting from pyrolysis of **3** at 220 °C and of the residues obtained after thermolysis of **4** at the following temperatures: 475 °C, 600 °C, 1200 °C; Figure S4: Solid-state ^{1}H and ^{13}C NMR spectra of **3** and **3@220**; Figure S5: ^{1}H and ^{13}C NMR spectra of **4** in CD_3CN solvent and **4@373** in CD_2Cl_2 solvent; Figure S6: N_2 sorption isotherms at −196 °C and CO_2 sorption isotherms at 0 °C of **4@1200**; Figure S7: Pore size distributions of **4@1200** as obtained by DFT analysis of the N_2 sorption isotherms at −196 °C and CO_2 sorption isotherms at 0 °C.

Accession Codes

CCDC-892809 (**2**), CCDC-892810 (**3**), and CCDC-1941506 (**4**) contain the supplementary crystallographic data for this paper. These data can be obtained free of charge via www.ccdc.cam.ac.uk/data_request/cif, or by emailing data_request@ccdc.cam.ac.uk, or by contacting The Cambridge Crystallographic Data Centre, 12 Union Road, Cambridge CB2 1EZ, UK; fax: +44 1223 336033.

ACKNOWLEDGMENTS

We warmly thank Dr. Philippe Gaveau and Mr. Emmanuel Fernandez from the Plateau Technique of the Institut Charles Gerhardt (UMR 5253 CNRS-ENSCM-UM, Université de Montpellier, Montpellier, France) for their help with the solid-state ^{1}H and ^{13}C NMR analyses described in this study. We are much indebted to Ms. Valérie Flaud from the Plateau Technique of the Institut Charles Gerhardt (UMR 5253 CNRS-ENSCM-UM, Université de Montpellier, Montpellier, France) for carrying out the XPS measurements reported herein, and to Dr. Erwan Oliviero from the Microscopie Électronique et Analytique (MEA) instrumentation platform (Université de Montpellier, Montpellier, France) for recording the HRTEM micrographs of the carbon samples. We are also thankful to Dr. Nicolas Brun from the Institut Charles Gerhardt (UMR 5253 CNRS-ENSCM-UM, Université de Montpellier, Montpellier, France) for helpful discussions regarding the gas-sorption data of **2@1200** and **4@1200**. Last, we express our gratitude to Prof. André Vioux from the Institut Charles Gerhardt (UMR 5253 CNRS-ENSCM-UM, Université de Montpellier, Montpellier, France) for providing valuable insight on the crystal engineering aspects of this paper.

REFERENCES

(1) Wegner, G. Topochemical reactions of monomers with conjugated triple bonds. I. Polymerization of derivatives of 2,4-hexadiyne-1,6-diols in the crystalline state. *Z. Naturforsch., B: Anorg. Chem. Org. Chem. Biochem. Biophys. Biol.* **1969**, *24*, 824-832.

(2) Baughman, R. H. Solid-State Synthesis of Large Polymer Single Crystals. *J. Polym. Sci., Polym. Phys. Ed.* **1974**, *12*, 1511-1535.

(3) Wegner, G. Solid-state polymerization mechanisms. *Pure Appl. Chem.* **1977**, *49*, 443-454.

(4) Enkelmann, V. Structural aspects of the topochemical polymerization of diacetylenes. *Adv. Polym. Sci.* **1984**, *63*, 91-136.

(5) Wegner, G. Topochemical reactions of monomers with conjugated triple bonds. IV. Polymerization of 2,4-hexadiyne-1,6-diol bis(p-toluenesulfonate). *Makromol. Chem.* **1971**, *145*, 85-94.

(6) Yee, K. C.; Chance, R. R. Synthesis and Properties of a New Polydiacetylene: Poly[1,6-di(*N*-Carbazolyl)-2,4-Hexadiyne]. *J. Polym. Sci., Polym. Phys. Ed.* **1978**, *16*, 431-441.

(7) Hirshfeld, F. L.; Schmidt, G. M. J. Topochemical Control of Solid-State Polymerization. *J. Polym. Sci., Part A: Gen. Pap.* **1964**, *2*, 2181-2190.

(8) Chance, R. R.; Patel, G. N. Solid-State Polymerization of a Diacetylene Crystal: Thermal, Ultraviolet, and γ-Ray Polymerization of 2,4-Hexadiyne-1,6-Diol *Bis*-(*p*-Toluene Sulfonate). *J. Polym. Sci., Polym. Phys. Ed.* **1978**, *16*, 859-881.

(9) Sixl, H. Spectroscopy of the intermediate states of the solid-state polymerization reaction in diacetylene crystals. *Adv. Polym. Sci.* **1984**, *63*, 49-90.

(10) Huntsman, W. D. In *The chemistry of functional groups, supplement C: the chemistry of triple-bonded functional groups Part 2*; Patai, S., Rappoport, Z., Eds.; Wiley: Chichester, U.K., 1983; Chapter 22, pp 917-980.

(11) Carré, F.; Devylder, N.; Dutremez, S. G.; Guérin, C.; Henner, B. J. L.; Jolivet, A.; Tomberli, V.; Dahan, F. Synthesis and X-ray Crystallographic Studies of Diacetylenic Molecules Bearing Triorganosilyl, Triorganostannyl, and Diorganophosphanyl Substituents. Investigation of Their Solid-State and Molten-State Polymerization. *Organometallics* **2003**, *22*, 2014-2033.

(12) Milburn, G. H. W.; Werninck, A.; Tsibouklis, J.; Bolton, E.; Thomson, G.; Shand, A. J. Synthesis and properties of some novel unsymmetrically substituted diacetylenes. *Polymer* **1989**, *30*, 1004-1007.

(13) Tsibouklis, J.; Campbell, C.; Werninck, A. R.; Shand, A. J.; Milburn, G. H. W. The thermal polymerization of a diacetylenic liquid crystal. *Polym. Bull.* **1992**, *29*, 661-668.

(14) Tsibouklis, J. The Liquid-Crystalline-State Polymerization of Diacetylenes. *Adv. Mater.* **1995**, *7*, 407-408.

(15) Fomina, L.; Allier, H.; Fomine, S.; Salcedo, R.; Ogawa, T. Synthesis and Molten-State Polymerization of Some Novel Conjugated Diacetylenes. *Polym. J.* **1995**, *27*, 591-600.

(16) Ogawa, T. Diacetylenes in polymeric systems. *Prog. Polym. Sci.* **1995**, *20*, 943-985.

(17) Dupont, J. On the Solid, Liquid and Solution Structural Organization of Imidazolium Ionic Liquids. *J. Braz. Chem. Soc.* **2004**, *15*, 341-350.

(18) Chiappe, C. Nanostructural Organization of Ionic Liquids: Theoretical and Experimental Evidences of the Presence of Well Defined Local Structures in Ionic Liquids. *Monatsh. Chem.* **2007**, *138*, 1035-1043.

(19) Costa Gomes, M. F.; Lopes, J. N. C.; Padua, A. A. H. Thermodynamics and Micro Heterogeneity of Ionic Liquids. *Top. Curr. Chem.* **2009**, *290*, 161-183.

(20) Dupont, J. From Molten Salts to Ionic Liquids: A "Nano" Journey. *Acc. Chem. Res.* **2011**, *44*, 1223-1231.

(21) Shimizu, K.; Tariq, M.; Freitas, A. A.; Pádua, A. A. H.; Lopes, J. N. C. Self-Organization in Ionic Liquids: From Bulk to Interfaces and Films. *J. Braz. Chem. Soc.* **2016**, *27*, 349-362.

(22) Hayes, R.; Warr, G. G.; Atkin, R. Structure and Nanostructure in Ionic Liquids. *Chem. Rev.* **2015**, *115*, 6357-6426.

(23) Russina, O.; Lo Celso, F.; Plechkova, N.; Jafta, C. J.; Appetecchi, G. B.; Triolo, A. Mesoscopic organization in ionic liquids. *Top. Curr. Chem. (Z)* **2017**, *375*, 58.

(24) Iwase, Y.; Kondo, K.; Kamada, K.; Ohta, K. Synthesis and Nonlinear Properties of Poly[1,4-bis(4-alkylpyridinium)butadiyne triflate]. *J. Polym. Sci., Part A: Polym. Chem.* **2001**, *39*, 3686-3691.

(25) Iwase, Y.; Kondo, K.; Kamada, K.; Ohta, K. 1,4-Addition Polymerization of 1,4-Bis(4-benzylpyridinium)butadiyne Triflate in a Dipolar Aprotic Solvent. *J. Polym. Sci., Part A: Polym. Chem.* **2002**, *40*, 3534-3541.

(26) Fahsi, K.; Dumail, X.; Dutremez, S. G.; van der Lee, A.; Vioux, A.; Viau, L. Diacetylenes with Ionic-Liquid-Like Substituents: Associating a Polymerizing Cation with a Polymerizing Anion in a Single Precursor for the Synthesis of N-Doped Carbon Materials. *Chem. - Eur. J.* **2016**, *22*, 1682-1695.

(27) Chougrani, K.; Deschamps, J.; Dutremez, S.; van der Lee, A.; Barisien, T.; Legrand, L.; Schott, M.; Filhol, J.-S.; Boury, B. Red Ionic Water-Soluble Imidazolium-Containing Polydiacetylene. *Macromol. Rapid Commun.* **2008**, *29*, 580-586.

(28) Walden, P. Molecular weights and electrical conductivity of several fused salts. *Bull. Acad. Imp. Sci. St.-Petersbourg* **1914**, *8*, 405-22.

(29) Benzigar, M. R.; Talapaneni, S. N.; Joseph, S.; Ramadass, K.; Singh, G.; Scaranto, J.; Ravon, U.; Al-Bahily, K.; Vinu, A. Recent advances in functionalized micro and mesoporous carbon materials: synthesis and applications. *Chem. Soc. Rev.* **2018**, *47*, 2680-2721.

(30) Lee, J. S.; Wang, X.; Luo, H.; Baker, G. A.; Dai, S. Facile Ionothermal Synthesis of Microporous and Mesoporous Carbons from Task Specific Ionic Liquids. *J. Am. Chem. Soc.* **2009**, *131*, 4596-4597.

(31) Yuan, J.; Giordano, C.; Antonietti, M. Ionic Liquid Monomers and Polymers as Precursors of Highly Conductive, Mesoporous, Graphitic Carbon Nanostructures. *Chem. Mater.* **2010**, *22*, 5003-5012.

(32) Paraknowitsch, J. P.; Thomas, A. Functional Carbon Materials From Ionic Liquid Precursors. *Macromol. Chem. Phys.* **2012**, *213*, 1132-1145.

(33) Fellinger, T.-P.; Thomas, A.; Yuan, J.; Antonietti, M. 25th Anniversary Article: "Cooking Carbon with Salt": Carbon Materials and Carbonaceous Frameworks from Ionic Liquids and Poly(ionic liquid)s. *Adv. Mater.* **2013**, *25*, 5838-5855.

(34) Sakaushi, K.; Antonietti, M. Carbon- and Nitrogen-Based Porous Solids: A Recently Emerging Class of Materials. *Bull. Chem. Soc. Jpn.* **2015**, *88*, 386-398.

(35) Paraknowitsch, J. P.; Zhang, J.; Su, D.; Thomas, A.; Antonietti, M. Ionic Liquids as Precursors for Nitrogen-Doped Graphitic Carbon. *Adv. Mater.* **2010**, *22*, 87-92.

(36) Lee, J. S.; Wang, X.; Luo, H.; Dai, S. Fluidic Carbon Precursors for Formation of Functional Carbon under Ambient Pressure Based on Ionic Liquids. *Adv. Mater.* **2010**, *22*, 1004-1007.

(37) Paraknowitsch, J. P.; Thomas, A.; Antonietti, M. A detailed view on the polycondensation of ionic liquid monomers towards nitrogen doped carbon materials. *J. Mater. Chem.* **2010**, *20*, 6746-6758.

(38) Fulvio, P. F.; Lee, J. S.; Mayes, R. T.; Wang, X.; Mahurin, S. M.; Dai, S. Boron and nitrogen-rich carbons from ionic liquid precursors with tailorable surface properties. *Phys. Chem. Chem. Phys.* **2011**, *13*, 13486-13491.

(39) Paraknowitsch, J. P.; Zhang, Y.; Thomas, A. Synthesis of mesoporous composite materials of nitrogen-doped carbon and silica using a reactive surfactant approach. *J. Mater. Chem.* **2011**, *21*, 15537-15543.

(40) Fellinger, T.-P.; Hasché, F.; Strasser, P.; Antonietti, M. Mesoporous Nitrogen-Doped Carbon for the Electrocatalytic Synthesis of Hydrogen Peroxide. *J. Am. Chem. Soc.* **2012**, *134*, 4072-4075.

(41) Zhang, S.; Miran, M. S.; Ikoma, A.; Dokko, K.; Watanabe, M. Protic Ionic Liquids and Salts as Versatile Carbon Precursors. *J. Am. Chem. Soc.* **2014**, *136*, 1690-1693.

(42) Zhang, S.; Dokko, K.; Watanabe, M. Direct Synthesis of Nitrogen-Doped Carbon Materials from Protic Ionic Liquids and Protic Salts: Structural and Physicochemical Correlations between Precursor and Carbon. *Chem. Mater.* **2014**, *26*, 2915-2926.

(43) Shirley, D. A. High-Resolution X-Ray Photoemission Spectrum of the Valence Bands of Gold. *Phys. Rev. B: Solid State* **1972**, *5*, 4709-4714.

(44) Scofield, J. H. Hartree-Slater subshell photoionization cross-sections at 1254 and 1487 eV. *J. Electron Spectrosc. Relat. Phenom.* **1976**, *8*, 129-137.

(45) Njus, J. M.; Sandman, D. J. Solid-state NMR and the thermal polymerization of 2,4-hexadiyne-1,6-diol *bis*-(*p*-toluenesulfonate). *Solid State Nucl. Magn. Reson.* **2006**, *29*, 251-257.

(46) Bierer, D. E.; Dener, J. M.; Dubenko, L. G.; Gerber, R. E.; Litvak, J.; Peterli, S.; Peterli-Roth, P.; Truong, T. V.; Mao, G.; Bauer, B. E. Novel 1,2-Dithiins: Synthesis, Molecular Modeling Studies, and Antifungal Activity. *J. Med. Chem.* **1995**, *38*, 2628-2648.

(47) Rougeau, L.; Picq, D.; Rastello, M.; Frantz, Y. New irreversible thermochromic polydiacetylenes. *Tetrahedron* **2008**, *64*, 9430-9436.

(48) Bruker, APEX3, SAINT, XPREP and SADABS, Bruker AXS Inc., Madison, Wisconsin, USA, 2016.

(49) Rigaku Oxford Diffraction, CrysAlis PRO, Rigaku Oxford Diffraction Ltd, Yarnton, England, 2017.

(50) van der Lee, A. Charge flipping for routine structure solution. *J. Appl. Crystallogr.* **2013**, *46*, 1306-1315.

(51) Palatinus, L.; Chapuis, G. *SUPERFLIP* - a computer program for the solution of crystal structures by charge flipping in arbitrary dimensions. *J. Appl. Crystallogr.* **2007**, *40*, 786-790.

(52) Betteridge, P. W.; Carruthers, J. R.; Cooper, R. I.; Prout, K.; Watkin, D. J. *CRYSTALS* version 12: software for guided crystal structure analysis. *J. Appl. Crystallogr.* **2003**, *36*, 1487.

(53) Cooper, R. I.; Thompson, A. L.; Watkin, D. J. *CRYSTALS* enhancements: dealing with hydrogen atoms in refinement. *J. Appl. Crystallogr.* **2010**, *43*, 1100-1107.

(54) Dolomanov, O. V.; Bourhis, L. J.; Gildea, R. J.; Howard, J. A. K.; Puschmann, H. *OLEX2*: a complete structure solution, refinement and analysis program. *J. Appl. Crystallogr.* **2009**, *42*, 339-341.

(55) Fahsi, K.; Deschamps, J.; Chougrani, K.; Viau, L.; Boury, B.; Vioux, A.; van der Lee, A.; Dutremez, S. G. Stability and solid-state polymerization reactivity of imidazolyl- and benzimidazolyl-substituted diacetylenes: pivotal role of lattice water. *CrystEngComm* **2013**, *15*, 4261-4279.

(56) Jenkins, I. H.; Kar, A. K.; Lindsell, W. E.; Murray, C.; Preston, P. N.; Wang, C.; Wherrett, B. S. Synthesis and Optical Characterization of Polydiacetylenes Containing Carboxylic Acid, Carbamate, Phosphonium, and Quaternary Ammonium Functionalities. *Macromolecules* **1996**, *29*, 6365-6370.

(57) Wait, E.; Powell, H. M. The Crystal and Molecular Structure of Tetraethylammonium Iodide. *J. Chem. Soc.* **1958**, 1872-1875.

(58) Vincent, B. R.; Knop, O.; Linden, A.; Cameron, T. S.; Robertson, K. N. Crystal chemistry of tetraradial species. Part 2. Crystal structures of Et_4NI, $Ph_4PBr{\cdot}H_2O$, and $Ph_4PBr{\cdot}2H_2O$. *Can. J. Chem.* **1988**, *66*, 3060-3069.

(59) Li, Q.; Mak, T. C. W. Inclusion Compounds of Thiourea and Peralkylated Ammonium Salts. III. Hydrogen-Bonded Host Lattices Built of Thiourea and Nitrate Ions. *Acta Crystallogr., Sect. B: Struct. Sci.* **1996**, *52*, 989-998.

(60) Henderson, W. A.; Herstedt, M.; Young, V. G., Jr.; Passerini, S.; De Long, H. C.; Trulove, P. C. New Disordering Mode for $TFSI^-$ Anions: The Nonequilibrium, Plastic Crystalline Structure of Et_4NTFSI. *Inorg. Chem.* **2006**, *45*, 1412-1414.

(61) McKinnon, J. J.; Jayatilaka, D.; Spackman, M. A. Towards quantitative analysis of intermolecular interactions with Hirshfeld surfaces. *Chem. Commun.* **2007**, 3814-3816.

(62) Spackman, M. A.; Jayatilaka, D. Hirshfeld surface analysis. *CrystEngComm* **2009**, *11*, 19-32.

(63) Spackman, P. R.; Turner, M. J.; McKinnon, J. J.; Wolff, S. K.; Grimwood, D. J.; Jayatilaka, D.; Spackman, M. A. *CrystalExplorer*: a program for Hirshfeld surface analysis, visualization and quantitative analysis of molecular crystals. *J. Appl. Crystallogr.* **2021**, *54*, 1006-1011.

(64) Fahsi, K.; Dutremez, S. G.; Vioux, A.; Viau, L. Azole-functionalized diacetylenes as precursors for nitrogen-doped graphitic carbon materials. *J. Mater. Chem. A* **2013**, *1*, 4451-4461.

(65) Rondeau-Gagné, S.; Morin, J.-F. Preparation of carbon nanomaterials from molecular precursors. *Chem. Soc. Rev.* **2014**, *43*, 85-98.

(66) Dokurno, P.; Łubkowski, J.; Błażejowski, J. Thermal properties, thermolysis and thermochemistry of alkanaminium iodides. *Thermochim. Acta* **1990**, *165*, 31-48.

(67) Iskakova, A. A.; Asanbaeva, N. B.; Gerasimov, K. B.; Uvarov, N. F.; Slobodyuk, A. B.; Kavun, V. Ya. Phase transitions and transport properties in tetra-n-butylammonium iodide. *Solid State Ionics*, 2019, **336**, 26-30.

(68) Liu, K.; Zhou, Y.-X.; Han, H.-B.; Zhou, S.-S.; Feng, W.-F.; Nie, J.; Li, H.; Huang, X.-J.; Armand, M.; Zhou, Z.-B. Ionic liquids based on (fluorosulfonyl)(pentafluoroethanesulfonyl)imide with various oniums. *Electrochim. Acta* **2010**, *55*, 7145-7151.

(69) Montanino, M.; Carewska, M.; Alessandrini, F.; Passerini, S.; Appetecchi, G. B. The role of the cation aliphatic side chain length in piperidinium bis(trifluoromethansulfonyl)imide ionic liquids. *Electrochim. Acta* **2011**, *57*, 153-159.

(70) Salgado, J.; Parajó, J. J.; Fernández, J.; Villanueva, M. Long-term thermal stability of some 1-butyl-1-methylpyrrolidinium ionic liquids. *J. Chem. Thermodyn.* **2014**, *74*, 51-57.

(71) Quraishi, K. S.; Bustam, M. A.; Krishnan, S.; Khan, M. I.; Wilfred, C. D.; Lévêque, J.-M. Thermokinetics of alkyl methylpyrrolidinium [NTf_2] ionic liquids - Effect of alkyl chain on thermal stability. *J. Therm. Anal. Calorim.* **2017**, *129*, 261-270.

(72) Ferdeghini, C.; Guazzelli, L.; Pomelli, C. S.; Ciccioli, A.; Brunetti, B.; Mezzetta, A.; Vecchio Ciprioti, S. Synthesis, thermal behavior and kinetic study of *N*-morpholinium dicationic ionic liquids by thermogravimetry. *J. Mol. Liq.* **2021**, *332*, 115662.

(73) Shiga, K.; Inoguchi, T.; Mori, K.; Kondo, K.; Kamada, K.; Tawa, K.; Ohta, K.; Maruo, T.; Mochizuki, E.; Kai, Y. Synthesis and Nonlinear Properties of Poly[1,4-bis(4-methylpyridinium)butadiyne triflate)]. *Macromol. Chem. Phys.* **2001**, *202*, 257-262.

(74) Holbrey, J. D.; Reichert, W. M.; Nieuwenhuyzen, M.; Johnston, S.; Seddon, K. R.; Rogers, R. D. Crystal polymorphism in 1-butyl-3-methylimidazolium halides: supporting ionic liquid formation by inhibition of crystallization. *Chem. Commun.* **2003**, 1636-1637.

(75) Holbrey, J. D.; Reichert, W. M.; Rogers, R. D. Crystal structures of imidazolium bis(trifluoromethanesulfonyl)imide 'ionic liquid' salts: the first organic salt with a *cis*-TFSI anion conformation. *Dalton Trans.* **2004**, 2267-2271.

(76) Lozynski, M.; Pernak, J.; Gdaniec, Z.; Gorska, B.; Béguin, F. Proof of ion-pair structures in ammonium-based protic ionic liquids using combined NMR and DFT/PCM-based chemical shift calculations. *Phys. Chem. Chem. Phys.* **2017**, *19*, 25033-25043.

(77) Tuinstra, F.; Koenig, J. L. Raman Spectrum of Graphite. *J. Chem. Phys.* **1970**, *53*, 1126-1130.

(78) Vidano, R.; Fischbach, D. B. New Lines in the Raman Spectra of Carbons and Graphite. *J. Am. Ceram. Soc.* **1978**, *61*, 13-17.

(79) Ferrari, A. C.; Robertson, J. Interpretation of Raman spectra of disordered and amorphous carbon. *Phys. Rev. B: Condens. Matter Mater. Phys.* **2000**, *61*, 14095-14107.

(80) Reich, S.; Thomsen, C. Raman spectroscopy of graphite. *Philos. Trans. R. Soc. London, Ser. A* **2004**, *362*, 2271-2288.

(81) Bokobza, L.; Bruneel, J.-L.; Couzi, M. Raman Spectra of Carbon-Based Materials (from Graphite to Carbon Black) and of Some Silicone Composites. *C* **2015**, *1*, 77-94.

(82) Wang, Y.; Alsmeyer, D. C.; McCreery, R. L. Raman Spectroscopy of Carbon Materials: Structural Basis of Observed Spectra. *Chem. Mater.* **1990**, *2*, 557-563.

(83) Merlen, A.; Buijnsters, J. G.; Pardanaud, C. A Guide to and Review of the Use of Multiwavelength Raman Spectroscopy for Characterizing Defective Aromatic Carbon Solids: from Graphene to Amorphous Carbons. *Coatings* **2017**, *7*, 153.

(84) Lespade, P.; Marchand, A.; Couzi, M.; Cruege, F. Caractérisation de matériaux carbonés par microspectrométrie Raman. *Carbon* **1984**, *22*, 375-385.

(85) Pimenta, M. A.; Dresselhaus, G.; Dresselhaus, M. S.; Cançado, L. G.; Jorio, A.; Saito, R. Studying disorder in graphite-based systems by Raman spectroscopy. *Phys. Chem. Chem. Phys.* **2007**, *9*, 1276-1291.

(86) Puech, P.; Kandara, M.; Paredes, G.; Moulin, L.; Weiss-Hortala, E.; Kundu, A.; Ratel-Ramond, N.; Plewa, J.-M.; Pellenq, R.; Monthioux, M. Analyzing the Raman Spectra of Graphenic Carbon Materials from Kerogens to Nanotubes: What Type of Information Can Be Extracted from Defect Bands? *C* **2019**, *5*, 69.

(87) Ferrari, A. C.; Rodil, S. E.; Robertson, J. Interpretation of infrared and Raman spectra of amorphous carbon nitrides. *Phys. Rev. B: Condens. Matter Mater. Phys.* **2003**, *67*, 155306.

(88) Ferrari, A. C.; Robertson, J. Raman spectroscopy of amorphous, nanostructured, diamond-like carbon, and nanodiamond. *Philos. Trans. R. Soc. London, Ser. A* **2004**, *362*, 2477-2512.

(89) Cançado, L. G.; Takai, K.; Enoki, T.; Endo, M.; Kim, Y. A.; Mizusaki, H.; Jorio, A.; Coelho, L. N.; Magalhães-Paniago, R.; Pimenta, M. A. General equation for the determination of the crystallite size L_a of nanographite by Raman spectroscopy. *Appl. Phys. Lett.* **2006**, *88*, 163106.

(90) Bulusheva, L. G.; Okotrub, A. V.; Kinloch, I. A.; Asanov, I. P.; Kurenya, A. G.; Kudashov, A. G.; Chen, X.; Song, H. Effect of nitrogen doping on Raman spectra of multi-walled carbon nanotubes. *Phys. Status Solidi B* **2008**, *245*, 1971-1974.

(91) Xu, L.; Cheng, L. Graphite Oxide under High Pressure: A Raman Spectroscopic Study. *J. Nanomater.* **2013**, 731875.

(92) Bautista-Flores, C.; Arellano-Peraza, J. S.; Sato-Berrú, R. Y.; Camps, E.; Mendoza, D. Sulfur and few-layer graphene interaction under thermal treatments. *Chem. Phys. Lett.* **2016**, *665*, 121-126.

(93) Gupta, V.; Nakajima, T.; Žemva, B. Raman scattering study of highly fluorinated graphite. *J. Fluorine Chem.* **2001**, *110*, 145-151.

(94) Ohana, I.; Palchan, I.; Yacoby, Y.; Davidov, D.; Selig, H. Raman scattering of stage 2 graphite fluorine intercalation compounds. *Solid State Commun.* **1985**, *56*, 505-508.

(95) Rao, A. M.; Fung, A. W. P.; di Vittorio, S. L.; Dresselhaus, M. S.; Dresselhaus, G.; Endo, M.; Oshida, K.; Nakajima, T. Raman-scattering and transmission-electron-microscopy studies of fluorine-intercalated graphite fibers C_xF ($7.8 \geq x \geq 2.9$). *Phys. Rev. B: Condens. Matter Mater. Phys.* **1992**, *45*, 6883-6892.

(96) Asanov, I. P.; Bulusheva, L. G.; Dubois, M.; Yudanov, N. F.; Alexeev, A. V.; Makarova, T. L.; Okotrub, A. V. Graphene nanochains and nanoislands in the layers of room-temperature fluorinated graphite. *Carbon* **2013**, *59*, 518-529.

(97) Zhou, L.; Zhou, L.; Wang, X.; Yu, J.; Yang, M.; Wang, J.; Peng, H.; Liu, Z. Trifluoromethylation of graphene. *APL Mater.* **2014**, *2*, 092505.

(98) Brouillette, D.; Irish, D. E.; Taylor, N. J.; Perron, G.; Odziemkowski, M.; Desnoyers, J. E. Stable solvates in solution of lithium bis(trifluoromethylsulfone)imide in glymes and other aprotic solvents: Phase diagrams, crystallography and Raman spectroscopy. *Phys. Chem. Chem. Phys.* **2002**, *4*, 6063-6071.

(99) Sadezky, A.; Muckenhuber, H.; Grothe, H.; Niessner, R.; Pöschl, U. Raman microspectroscopy of soot and related carbonaceous materials: Spectral analysis and structural information. *Carbon* **2005**, *43*, 1731-1742.

(100) X-ray Photoelectron Spectroscopy (XPS) Reference Pages_ Organic Sulphur. Accessed September 15, 2022. http://www.xpsfitting.com/2014/04/organic-sulphur.html.

(101) Yang, Z.; Yao, Z.; Li, G.; Fang, G.; Nie, H.; Liu, Z.; Zhou, X.; Chen, X.; Huang, S. Sulfur-Doped Graphene as an Efficient Metal-free Cathode Catalyst for Oxygen Reduction. *ACS Nano* **2012**, *6*, 205-211.

(102) Su, Y.; Zhang, Y.; Zhuang, X.; Li, S.; Wu, D.; Zhang, F.; Feng, X. Low-temperature synthesis of nitrogen/sulfur co-doped three-dimensional graphene frameworks as efficient metal-free electrocatalyst for oxygen reduction reaction. *Carbon* **2013**, *62*, 296-301.

(103) Zhou, G.; Paek, E.; Hwang, G. S.; Manthiram, A. Long-life Li/polysulphide batteries with high sulphur loading enabled by lightweight three-dimensional nitrogen/sulphur-codoped graphene sponge. *Nat. Commun.* **2015**, *6*, 7760.

(104) Zeng, P.; Han, Y.; Duan, X.; Jia, G.; Huang, L.; Chen, Y. A stable graphite electrode in superconcentrated LiTFSI-DME/DOL electrolyte and its application in lithium-sulfur full battery. *Mater. Res. Bull.* **2017**, *95*, 61-70.

(105) Siow, K. S.; Britcher, L.; Kumar, S.; Griesser, H. J. XPS Study of Sulfur and Phosphorus Compounds with Different Oxidation States. *Sains Malays.* **2018**, *47*, 1913-1922.

(106) Gursu, H.; Gencten, M.; Sahin, Y. Preparation of Sulphur-Doped Graphene-Based Electrodes by Cyclic Voltammetry: A Potential Application for Vanadium Redox Flow Battery. *Int. J. Electrochem. Sci.* **2018**, *13*, 875-885.

(107) X-ray Photoelectron Spectroscopy (XPS) Reference Pages_ Fluorine. Accessed September 15, 2022. http://www.xpsfitting.com/2017/05/fluorine.html.

(108) Nansé, G.; Papirer, E.; Fioux, P.; Moguet, F.; Tressaud, A. Fluorination of carbon blacks: an X-ray photoelectron spectroscopy study: I. A literature review of XPS studies of fluorinated carbons. XPS investigation of some reference compounds. *Carbon* **1997**, *35*, 175-194.

(109) Lee, J.-W.; Jeong, S.-P.; You, N.-H.; Moon, S.-Y. Tunable Synthesis of Predominant Semi-Ionic and Covalent Fluorine Bonding States on a Graphene Surface. *Nanomaterials* **2021**, *11*, 942.

(110) Wu, X.; Xu, M.; Wang, S.; Abbas, K.; Huang, X.; Zhang, R.; Tedesco, A. C.; Bi, H. F,N-Doped carbon dots as efficient Type I photosensitizers for photodynamic therapy. *Dalton Trans.* **2022**, *51*, 2296-2303.

(111) Ullah, S.; Shi, Q.; Zhou, J.; Yang, X.; Ta, H. Q.; Hasan, M.; Ahmad, N. M.; Fu, L.; Bachmatiuk, A.; Rümmeli, M. H. Advances and Trends in Chemically Doped Graphene. *Adv. Mater. Interfaces* **2020**, *7*, 2000999.

(112) Mallet-Ladeira, P.; Puech, P.; Toulouse, C.; Cazayous, M.; Ratel-Ramond, N.; Weisbecker, P.; Vignoles, G. L.; Monthioux, M. A Raman study to obtain crystallite size of carbon materials: A better alternative to the Tuinstra-Koenig law. *Carbon* **2014**, *80*, 629-639.

(113) Puech, P.; Dabrowska, A.; Ratel-Ramond, N.; Vignoles, G. L.; Monthioux, M. New insight on carbonisation and graphitisation mechanisms as obtained from a bottom-up analytical approach of X-ray diffraction patterns. *Carbon* **2019**, *147*, 602-611.

(114) Roisnel, T.; Rodríguez-Carvajal, J. WinPLOTR: A Windows Tool for Powder Diffraction Pattern Analysis. *Mater. Sci. Forum* **2001**, *378-381*, 118-123.

(115) Oberlin, A. Carbonization and graphitization. *Carbon* **1984**, *22*, 521-541.

(116) Rouzaud, J. N.; Oberlin, A. Structure, microtexture, and optical properties of anthracene and saccharose-based carbons. *Carbon* **1989**, *27*, 517-529.

(117) Beda, A.; Vaulot, C.; Matei Ghimbeu, C. Hard carbon porosity revealed by the adsorption of multiple gas probe molecules (N_2, Ar, CO_2, O_2 and H_2). *J. Mater. Chem. A* **2021**, *9*, 937-943.

(118) Carrasco-Marín, F.; López-Ramón, M. V.; Moreno-Castilla, C. Applicability of the Dubinin-Radushkevich Equation to CO_2 Adsorption on Activated Carbons. *Langmuir* **1993**, *9*, 2758-2760.

LEGENDS

Scheme 1. Schematic representation of the topochemical principle for diacetylene polymerization

Scheme 2. Syntheses of compounds 1-4

Figure 1. View along the *b* axis showing the organization of **2** in the solid state.

Figure 2. Charge-assisted hydrogen bonds and C-H$\cdots\pi$ interactions in crystalline **2**.

Figure 3. View along the *b* axis showing the organization of **3** in the solid state.

Figure 4. H-bond interactions between one nitrate anion and five DA molecules.

Figure 5. View along the *c* axis showing the organization of **4** in the solid state.

Figure 6. Relative contributions of various intermolecular interactions to the Hirshfeld surface areas of the diacetylenic cations in compounds **2-4**.

Figure 7. TG plot of **2** (a), DSC plot of **2** (b), TG plot of **3** (c), DSC plot of **3** (d), TG plot of **4** (e), DSC plot of **4** (f).

Figure 8. Raman spectra (λ_{ex} = 1064 nm) of as-synthesized **4** (a), **4** heated to 80 °C with concomitant UV irradiation (b), **4** heated to 120 °C with simultaneous UV irradiation (c), **4** heated to 170 °C on a DSC stage for a few minutes (d), and **4** heated to 170 °C on a DSC stage for 1 h (e).

Figure 9. Raman spectra (λ_{ex} = 785 nm) of the residues obtained after thermolysis of **2** at the following temperatures: 220 °C (a), 350 °C (b), 400 °C (c), 600 °C (d), 1200 °C (e).

Figure 10. X-ray powder patterns of the residues obtained after thermolysis of **2** at the following temperatures: 220 °C (a), 350 °C (b), 400 °C (c), 600 °C (d), 1200 °C (e).

Figure 11. HRTEM micrographs of **2@1200** (a) and **4@1200** (b). In each micrograph, a line profile analysis of one well-defined graphitic domain (outlined by a red rectangle) has been carried out, and the corresponding results are shown in (c) (**2@1200**) and (d) (**4@1200**).

Figure 12. Solid-state ^{1}H and ^{13}C NMR spectra of **2** ((a) and (c)) and **2@220** ((b) and (d)). Peaks marked with an asterisk are spinning sidebands. In spectrum (d), the right-hand side spinning sideband overlaps with the resonance signals at $\delta \approx 50$ ppm.

Figure 13. N_2 sorption isotherms at −196 °C (a) and CO_2 sorption isotherms at 0 °C (b) of **2@1200**.

Figure 14. Pore size distributions of **2@1200** as obtained by DFT analysis of the N_2 sorption isotherms at −196 °C (a) and CO_2 sorption isotherms at 0 °C (b).

Table 1. Crystal data and experimental details of data collection and refinement for compounds 2-4

	2	3	4
formula sum	$C_{18}H_{34}I_2N_2$	$C_{18}H_{34}N_4O_6$	$C_{22}H_{34}F_{12}N_4O_8S_4$
formula moiety	$C_{18}H_{34}N_2$, 2 I	$C_{18}H_{34}N_2$, 2 NO_3	$C_{18}H_{34}N_2$, 2 $C_2F_6NO_4S_2$
***T* (K)**	173	173	173
space group	$P2_1/c$	$P2_1/n$	$P2_1/n$
crystal system	monoclinic	monoclinic	monoclinic
***a* (Å)**	8.83360(10)	16.1510(8)	11.0214(3)
***b* (Å)**	6.81940(10)	6.8539(4)	14.0558(4)
***c* (Å)**	17.6886(3)	19.0176(9)	11.4263(3)
α (°)	90	90	90
β (°)	93.5553(16)	90.820(5)	96.1465(11)
γ (°)	90	90	90
***V* (Å^3)**	1063.508(18)	2104.99(19)	1759.93(5)
Z	2	4	2
ρ (g cm^{-3})	1.662	1.270	1.583
fw (g mol^{-1})	532.27	402.49	838.77
μ (mm^{-1})	2.958	0.095	3.521
***R*$_{int}$**	0.023	0.020	0.069
θ_{max} (°)	29.119	28.942	72.649
resolution (Å)	0.73	0.73	0.81
***N*$_{tot}$ (measured)**	26586	8692	61806
***N*$_{ref}$ (unique)**	2687	4787	3498
***N*$_{ref}$ ($I > 2\sigma(I)$)**	2487	3618	3111
***N*$_{ref}$ (least-squares)**	2487	4787	3111
***N*$_{par}$**	100	253	226
$\langle\sigma(I)/I\rangle$	0.0473	0.0733	0.0223
***R*$_1$ ($I > 2\sigma(I)$)**	0.0201	0.0465	0.0381
***wR*$_2$ ($I > 2\sigma(I)$)**	0.0166	0.1007	0.0403
***R*$_1$ (all)**	0.0237	0.0667	0.0428
***wR*$_2$ (all)**	0.0169	0.1160	0.0480
GOF	1.1704	0.9198	1.0361
$\Delta\rho$ (e Å^{-3})	–0.80/1.69	–0.33/0.68	–0.41/0.33
crystal size (mm^3)	0.05 × 0.15 × 0.30	0.20 × 0.25 × 0.30	0.05 × 0.08 × 0.12

Table 2. Raman, X-ray diffraction, and elemental analysis results of the residues obtained by pyrolysis of 2-4

Sample	D band (cm^{-1})	G band (cm^{-1})	I_D/I_G	$d_{(002)}$ (Å)	L_c (Å)[a]	L_a (Å)[b]	N content (wt %)[c]	H content (wt %)[c]
2@220	1336	1572	1.22	-	-	-	5.20	5.22
2@350	1336	1572	1.39	4.15	9	-	4.06	5.12
2@400	1336	1572	1.60	4.24	9	-	4.03	4.97
2@600	1331	1577	1.72	3.76	11	15	3.68	3.16
2@1200	1306	1594	2.37	3.73	9	27	1.75	1.08
3@220	1344	1573	1.17	-	-	-	8.59	3.67
4@373	[d]	[d]	-	-	-	-	-	-
4@475	1247, 1337[e]	1454, 1585[e]	[f]	3.55	18	-	2.39	3.34
4@600	1332	1587	[f]	3.43	15	19	2.31	2.84
4@1200	1197, 1311[e]	1486, 1606[e]	[f]	3.80	11	28	1.40	0.42

[a]Calculated from the FWHM of the (002) peak. [b]Calculated from the FWHM of the (10) line. [c]Determined by C, H, N elemental analysis. [d]No identifiable peak. [e]Position of the major peak. [f]Not calculated due to the presence of several bands.

Table 3. XPS data of 2@1200 and 4@1200

2@1200		
Element	Content (atom %)	BE (eV) / assignment / ratio
N	0.61	398.3 / pyridinic N / 36
		400.8 / quaternary-graphitic N / 64
I	0.0	-
4@1200		
Element	Content (atom %)	BE (eV) / assignment / ratio
N	0.39	398.5 / pyridinic N / 41
		401.1 / quaternary-graphitic N / 59
F	0.46	686.2 / semi-ionic C-F / 74
		688.9 / CF_3 / 26
S	1.03	163.8 and 165.0 / C-S-C / 76
		164.6 and 165.8 / S-O / 10
		168.1 and 169.5 / C-SO_x-C (x = 2, 3) / 14

Table 4. N_2 and CO_2 physisorption data of 2@1200 and 4@1200

N_2						
Sample	S_{BET} (m^2 g^{-1})	C_{BET}	S_{micro} (m^2 g^{-1})[a]	V_{tot} (cm^3 g^{-1})	V_{micro} (cm^3 g^{-1})[a]	Pore widths (nm)[b]
2@1200	88	1447	82	0.051	0.031	0.53; 0.8; 0.95; 1.35; 1.6
4@1200	33	14	0	0.037	0	0.6; 1.6; 3; 5
CO_2						
Sample	S_{BET} (m^2 g^{-1})	C_{BET}	S_{DA} (m^2 g^{-1})[c]	V_{tot} (cm^3 g^{-1})	V_{DA} (cm^3 g^{-1})[c]	Pore widths (nm)[b]
2@1200	321	72	364	0.093	0.14	0.42; 0.51; 0.62; 0.79
4@1200	58	21	67	0.010	0.03	0.54; 0.61; 0.68; 0.80

[a]As determined by the *t*-plot method. [b]Calculated using DFT methods. [c]As determined by the Dubinin-Astakhov method.

SUBJECTS: ionic diacetylene, tetraalkylammonium, ionic liquid, crystal structure, supramolecular interactions, thermolysis, topochemical polymerization, liquid-state polymerization, polydiacetylene, polyelectrolyte, carbon materials

For Table of Contents Use Only

Symmetrical diacetylenes outfitted with ionic liquid-like groups: structural, polymerization, and carbonization studies

Karim Fahsi, Xavier Dumail, Lydie Viau, Arie van der Lee, Nathalie Masquelez, Dominique Granier, Cyril Vaulot, and Sylvain Georges Dutremez*

TOC Graphic

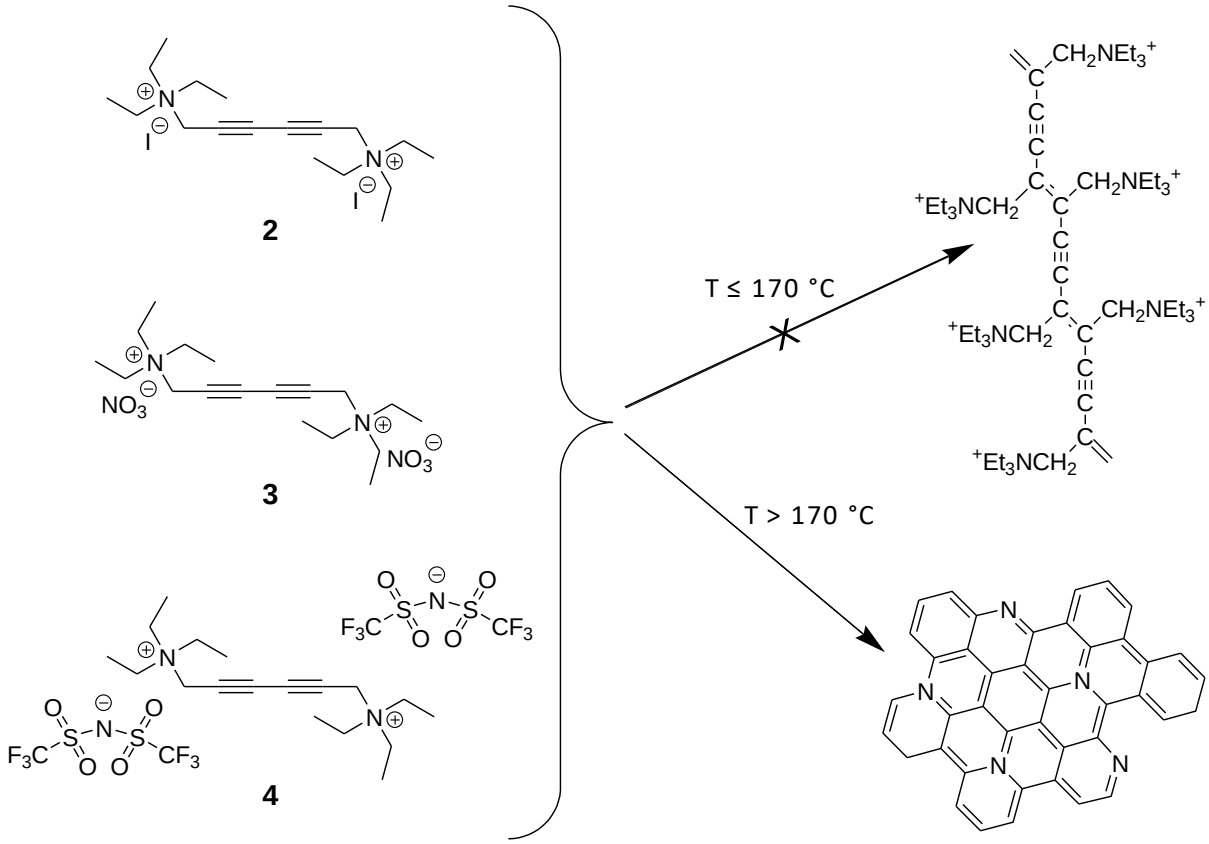

Synopsis

Three symmetrical diacetylenes bearing tetraalkylammonium substituents have been prepared, namely 1,6-bis(triethylammonium)hexa-2,4-diyne diiodide (**2**), dinitrate (**3**), and bis[bis(trifluoromethylsulfonyl)imide] (**4**). Compounds **2** and **3** are infusible solids and **4** is an ionic liquid. For these three salts, the duality between polymerization and carbonization has been investigated, and the results have been rationalized in terms of solid-state organization and molecular structure.